Observatório Nacional

Divisão de Programas de Pós-Graduação

MÉTODOS DE INVERSÃO DE DADOS MAGNÉTICOS PARA ESTIMAR FONTES REGIONAIS

Marlon Cabrera Hidalgo-Gato

Tese apresentada ao Programa de Pós-graduação em Geofísica do Observatório Nacional, como parte dos requisitos necessários à obtenção do Título de Doutor em Geofísica.

Orientador: Dra. Valéria Cristina F. Barbosa

Co-orientador: Dr. Vanderlei Coelho Oliveira Jr.

Rio de Janeiro

Dezembro de 2019

MÉTODOS DE INVERSÃO DE DADOS MAGNÉTICOS PARA ESTIMAR FONTES REGIONAIS

Marlon Cabrera Hidalgo-Gato

TESE SUBMETIDA AO PROGRAMA DE PÓS-GRADUAÇÃO EM GEOFÍSICA DO OBSERVATÓRIO NACIONAL COMO PARTE DOS REQUISITOS NECESSÁRIOS PARA A OBTENÇÃO DO TÍTULO DE DOUTOR EM GEOFÍSICA.

_____

Dra. Valéria Cristina Ferreira Barbosa (ON/MCTI)
Orientadora

_____

Dr. Vanderlei Coelho de Oliveira Junior (ON/MCTI)
Coorientador

_____

Dr. Cosme Ferreira Da Ponte Neto (ON/MCTI)

_____

Dr. Paulo de Tarso L. Menezes (UERJ/PETROBRAS)

_____

Dr. Julio Cesar S. de Oliveira Lyrio (PETROBRAS)

RIO DE JANEIRO, RJ - BRASIL
DEZEMBRO DE 2019

Cabrera Hidalgo-Gato, Marlon

Métodos de inversão 3D de fontes regionais a partir de dados magnéticos /Marlon Cabrera Hidalgo-Gato. – Rio de Janeiro: ON/MCTI, 2019.

XII, xx p.: il.; 29,7 cm.

Orientador: Dra. Valéria Cristina Ferreira Barbosa

Tese (doutorado) – ON/Programa de Pós-graduação em Geofísica, 2019.

Referências Bibliográficas: p. 62 – 64.

1. Métodos Potenciais. 2. Processamento de Sinais 3. Inversão magnética. I. Ferreira Barbosa, Valéria Cristina. II. Observatório Nacional/MCTI, Programa de Pós-graduação em Geofísica. III. Métodos de inversão 3D de fontes regionais a partir de dados magnéticos /Marlon Cabrera Hidalgo-Gato. – Rio de Janeiro: ON/MCTI, 2019.

Aos meus pais

Agradecimentos

Agradeço a minha família e, principalmente a meus pais por todo o apoio e confiança durante esta jornada.

A minha orientadora Dra. Valéria C. F. Barbosa, por confiar e incentivar esta divertida jornada de aprendizado.

Ao Observatório Nacional e a todos os professores e colaboradores do instituto.

Aos membros da banca por aceitarem avaliar e aperfeiçoar a finalização deste trabalho.

Resumo da Tese apresentada ao Programa de Pós-graduação em Geofísica do Observatório Nacional como parte dos requisitos necessários para a obtenção do título de Doutor em Geofísica.

MÉTODOS DE INVERSÃO DE DADOS MAGNÉTICOS PARA ESTIMAR FONTES REGIONAIS

Marlon Cabrera Hidalgo-Gato

Dezembro/2019

No contexto dos estudos de bacias sedimentares, apresentamos duas inversões magnéticas 3D rápidas e regularizadas no domínio espacial. A primeira inverte a anomalia de campo total para a estimativa da profundidade do embasamento, enquanto a segunda inverte a amplitude do vetor da anomalia magnética para estimar a intensidade da magnetização e a profundidade do embasamento. Ambas inversões discretizam as rochas do embasamento por um grid de prismas 3D verticais e justapostos nas direções horizontais cujas profundidades até o topo se aproximam das profundidades da topografia do embasamento em pontos discretos. Além disso, ambas inversões assumem sedimentos não magnéticos sobrepostos às rochas do embasamento magnético com magnetização constante. Propomos uma nova maneira de calcular a modelagem direta de um prisma, denominada modelagem direta prismática rápida. Essa modelagem direta rápida calcula as componentes do vetor de magnetização gerado por um prisma mediante uma integral 1D de dipolos ao longo da espessura do prisma, que, por sua vez, é multiplicada pela área horizontal do prisma. Essa abordagem reduz o tempo computacional não apenas do cálculo do modelo direto dos prismas, mas também da inversão não linear. Para inverter a anomalia de campo total, a direção e a intensidade da magnetização devem ser conhecidas. Assumimos uma intensidade de magnetização constante e conhecida e determinamos a declinação e inclinação do vetor de magnetização, realizando uma busca discreta e sistemática por

valores ótimos que minimizem a função de desajuste dos dados. Na inversão da anomalia de campo total para estimar a profundidade do embasamento, usamos a regularização de Tikhonov de primeira ordem. Na inversão da amplitude do vetor de anomalia magnética, para estimar simultaneamente a intensidade magnética e a profundidade do embasamento magnético, impomos a proximidade entre as profundidades estimadas e a profundidade média do relevo do embasamento. Mostramos que a inversão da anomalia de campo total é altamente dependente do conhecimento da direção do vetor de magnetização. Por outro lado, mostramos que a inversão da amplitude do vetor da anomalia magnética é fracamente dependente da direção do vetor de magnetização. Na última inversão, não é necessário nenhum conhecimento prévio sobre a direção do vetor de magnetização (declinação e inclinação). Testes em dados sintéticos e de campo das bacias do Pará-Maranhão e Foz do Amazonas (Brasil) comprovam a aplicabilidade de ambos os métodos propostos.

Abstract of the Thesis presented to the National Observatory´s Graduate Program in Geophysics as partial fulfillment of the requirements for the degree of Doctor in Geophysics.

MAGNETIC INVERSION METHODS FOR ESTIMATING REGIONAL SOURCES

Marlon Cabrera Hidalgo-Gato

Dezembro/2019

In the context of sedimentary basin studies, we present two fast 3D regularized magnetic inversions in the space domain. The first one inverts the total-field anomaly for depth-to-basement estimate whereas the second one inverts the amplitude of the magnetic anomaly vector to estimate both the magnetic intensity and the depth to the basement. Both inversions discretize the basement rocks by a grid of 3D vertical prisms juxtaposed in the horizontal directions whose depths to the tops approximate the depths to the basement topography at discrete points. Additionally, both inversions assume that nonmagnetic sediments overlay constant magnetized basement rocks. We propose a novel way to compute the forward modeling of a prism, named fast-prismatic forward modeling. This fast-prismatic forward modeling calculates the components of the magnetic vector yielded by a prism by a 1D integral of dipoles along the prism thickness, which, in turn, is multiplied by the horizontal area of the prism. This approach reduces the computational time not only of the prism forward model but also of the nonlinear inversion. To invert the total-field anomaly, the magnetization direction and intensity must be known. We assume a constant and known magnetization intensity and determine the declination and inclination of the magnetization vector by performing a discrete and systematic search for optimum values that minimizes the data-misfit function. In the total-field anomaly inversion for estimating the depth to the basement, we use the first-order Tikhonov regularization. In the amplitude of the magnetic anomaly vector inversion for simultaneously estimating the magnetic intensity and the depth to the magnetic basement, we impose the proximity between the estimated depths and the average depth of the basement

relief. We show that the total-field anomaly inversion is highly dependent on the knowledge of the magnetization vector direction. Conversely, we show that the inversion of the amplitude of the magnetic anomaly vector is weakly dependent on the magnetization vector direction. In the latter inversion, no previous knowledge about the direction of magnetization vector (declination, inclination) is required. Tests on synthetic and field data from the Pará-Maranhão and Foz do Amazonas Basins (Brazil) prove the applicability of both proposed methods.

List of Contents

List of Figures

Chapter 1

1.0 Introduction

Geophysics inverse problems consist in estimating an unknown vector parameter from a collection of observed data. These geophysical problems are ill-posed and thus, their solution is neither unique nor stable. The inverse problems could be divided into two main groups depending on the parameters we want to estimate: physical-property and structural inversion problems. The former estimates a physical-property distribution given a fixed geometry (e.g. RICHARDS et al., 1967; PARKER et al., 1987; BARBOSA and SILVA, 1994; LI and OLDENBURG, 1996; PORTNIAGUINE and ZHDANOV, 2002; CARATORI TONTINI et al., 2003; BARBOSA and SILVA, 2006; FARQUHARSON, 2008; SILVA DIAS et al., 2009; 2011; UIEDA and BARBOSA, 2012; IALONGO et al., 2014; UIEDA and BARBOSA, 2017). In contrast, the structural inverse problem estimates the source geometry assuming known physical-property contrast (e.g., ZEYEN AND POUS, 1991; MICKUS and PEEPLES, 1992; BARBOSA et al., 1997; 1999A; 1999B; NUNES et al., 2008; MARTINS et al., 2011; OLIVEIRA JR et al., 2011; BARNES and BARRAUD, 2012; OLIVEIRA JR and BARBOSA, 2013;). One of the main computational obstacles of both physical-property and structural inverse problems is the computational effort required to calculate the forward modeling with a large number of parameters.

The most common magnetic inversions parametrize the Earth's subsurface into a grid of prisms (2D or 3D) to estimate a magnetic-intensity distribution subject to fit the magnetic anomaly within a given degree of accuracy. However, the magnetic anomaly produced by a single prism (BHATTACHARYYA, 1964) is computationally

costly and complex because it involves a series of summations over trigonometric functions. In some cases, the geological source could be discretized by a sum of a series of dipoles, which leads to a simpler and faster calculation of the magnetic components than the forward modeling, which uses the prism-based discretization of the Earth's subsurface. PORTNIAGUINE and ZHDANOV (2002) and PILKINGTON (2016) parametrized the Earth's subsurface into a grid of dipoles to estimate the shape of geological sources by inverting the total-field anomaly. PILKINGTON (2016) calculated the magnetic forward modeling in the wavenumber domain, whereas PORTNIAGUINE and ZHDANOV (2002) calculated it in the space domain. CARATORI TONTINI et al. (2003) also used prismatic parameterization of the subsurface; however, they employed an approximation of the source distribution by means of positive constrained Gaussian functions.

On the other hand, if the geometries of geological sources are estimated by inverting the magnetic anomaly, a nonlinear system needs to be solved and hence the forward modeling must be calculated at each iteration. In practice, this means that several time-consuming iterative processes must be run to find a suitable solution. This is the case of estimating the depths to the magnetic basement of a sedimentary basin by means of magnetic anomaly data inversion.

The magnetic data in basin-scale studies have been used to delineate structural features within basement (e.g. structural highs and lows, terraces, ridges, faults, among others) yielding a structural map (e.g., CARVALHO et al., 2012; LORENÇO et al., 2014; HIDALGO-GATO and BARBOSA, 2015; ALI et al., 2017). The tectonic processes sculpt the basement structures, which, in turn, control the basin architecture. Hence, the structural framework of the basement in depth is important to understand the basin evolution and to assist the hydrocarbon exploration. The spectral analysis of the magnetic data has been widely used to estimate the average depths of ensembles of shallow- and deep-seated magnetic sources (SPECTOR and GRANT, 1970; OKUBO et al., 1985 and BANSAL et al., 2011) where the shallow-seated magnetic sources can be intrasedimentary mafic and ultramafic bodies and the deep-seated magnetic sources can be the basement. OKUBO et al. (1985) derived a method of estimating the average of the top and bottom of the deep-seated magnetic sources from the power spectrum of the total-field anomaly data. To estimate the entire basement topography rather than the average depths of the basement rocks, the main magnetic data inversions are grounded on the forward modeling proposed by PARKER (1973).

PARKER (1973), in a seminal paper, gave an equation that correlates the Fourier transform of the total-field anomaly with the Fourier transform of the power of the depths. Parker's formulation requires a previous knowledge about the average depth of the interface to overcome the intrinsic ambiguity involving the product of the physical property by the volume of the inversion of potential-field data that has been treated by SKEELS (1947) and BARBOSA et al. (2002), among others. Originally, it assumes a constant magnetization contrasts along the entire surface. However, extension to incorporate lateral variation of magnetization distribution presents no theoretical difficult in Parker's forward modeling since the magnetization distribution is known. Because Parker's forward modeling requires a series of Fourier transforms, both the data (total-field anomaly) and the depths describing the magnetic basement topography at discrete points must be located on a regular grid. The main advantages of the inverse methods based on Parker's wavenumber domain expansion formulation are 1) the faster calculation of the forward model and 2) the low computational load. On the other hand, one disadvantage of this formulation is the large smoothing imposed to the depth-to-basement estimates, because the inversion methods based on PARKER (1973) stabilize the solutions either by applying a low-pass filter to the data or by introducing a damping parameter. We call the methods that use PARKER (1973) forward method as "spectral inversions". Some examples of spectral inversions are: OLDENBURG (1974); GUSPÍ (1993); CARATORI TONTINI et al. (2008), among others. Using a non-spectral approach, some methods (e.g., MICKUS and PEEPLES, 1992; ZEYEN and POUS, 1991; GALLARDO-DELGADO et al., 2003; NUNES et al., 2008; HIDALGO-GATO and BARBOSA, 2019) parameterize the basement into a grid of prisms (2D or 3D) to estimate the shape of the basement topography subject to fit the observed total-field anomaly in the space domain.

In a nonlinear inversion, linear systems can be solved at several iterations to estimate a set of parameters. In geophysics, solving several linear systems usually involves a large non-sparse matrix. Hence, the solution of large-scale nonlinear inversions is a challenge because, usually, it deals with a considerable number of parameters and observations. For the gravity inversion, BOTT (1960) overcame this problem by using an analytical formula to update the parameters without requiring solving any linear system at each iteration. SILVA et al. (2014) shown that the BOTT (1960) method is, in fact, a particular case of the Gauss-Newton method that requires a positive (+1) or negative (-1) correlation between the parameters to be estimated and

the data misfit. UIEDA and BARBOSA (2017) extended the Gauss-Newton formulation of BOTT'S (1960) method to use tesseroids as model elements and Tikhonov regularization in order to estimate the Moho depth for the South American continent using satellite gravity data and seismological data. The requirement of correlation of +1 or -1 between the parameters and the predicted data is always satisfied in the gravity inversion. However, in the magnetic inversion, this correlation is only archived if the total magnetization vector is vertical.

In Chapter 2, we present a fast-nonlinear magnetic inversion to estimate the magnetic basement depth by following a non-spectral approach, this chapter was published by HIDALGO-GATO and BARBOSA (2019). We parametrize the basement layer as a grid of 3D vertical prisms juxtaposed in the horizontal directions with a known magnetization intensity. The tops of the prisms are the unknown parameters to be estimated from the total-field anomaly and represent the depths to the magnetic basement. For simplicity, the ith depth of the sedimentary basement to be estimated is directly located beneath the ith magnetic station. Here, we overcome two hurdles: 1) the time-consuming magnetic forward modeling and 2) the need of solving large non-sparse linear system iteratively. To overcome the computational cost of the magnetic forward modeling, we propose a strategy that does not require the computation of the magnetic anomalies produced by prisms through 3D integrals (BHATTACHARYYA, 1964). We replace the 3D integral used to calculate the total-field anomaly of a prism by a 1D integral along the prism thickness, considering the magnetic moment as the product of the magnetization intensity and the horizontal cross-section area of the prism. The 1D integral is calculated considering its lower and upper limits of the integration as the depth to the basement and the depth that may describe the non-magnetic bottom, respectively. Here, the 1D integral is calculated numerically using the Gauss-Legendre quadrature (GLQ) produced by dipoles located along the vertical axis passing through the prism center. Hereafter, we will refer to this proposed magnetic forward modeling as fast-prismatic forward modeling. To overcome the need of solving large non-sparse linear system iteratively, the full sensitivity matrix is not computed; rather, only the diagonal elements are calculated. In other words, the ith element of the ith row of the sensitivity matrix only needs to be computed leading to a diagonal sensitivity matrix. To estimate the basement relief from the total-field anomaly inversion, we first need to know the magnetization vector of the basement (its intensity and direction). By assuming the knowledge about the

magnetization intensity provided from the basement rocks, we determine the magnetization direction (inclination and declination) of the basement. We perform a systematic and non-automatic search of the data-misfit function on the plane of the inclination versus declination to map the optimum pair of inclination and declination as the one that yields the lowest value of the data-misfit function. Tests on synthetic data and on airborne magnetic data collected over an area of the Pará-Maranhão Basin, offshore northern Brazil, support the efficiency of our method in retrieving the basement relief of this poorly studied area of the Brazilian equatorial margin.

A drawback of the method presented in the Chapter 2 is the need to know the magnetization vector of the basement. The total-field anomaly inversion requires the knowledge about the total magnetization vector of the sources. Usually, geophysicists assume a purely-induced magnetization. If this assumption is not satisfied, erroneous depth-to-basement estimates are obtained from total-field anomaly inversion; hence, the remanent magnetization cannot be neglected.

Conversely, the amplitude of the magnetic anomaly vector is weakly dependent on the magnetization direction (SHEARER and LI, 2004; LI et al., 2010). The amplitude of the magnetic anomaly vector is defined as the square root of the sum of the squares of the $x-$, $y-$ and $z-$components of the magnetic anomaly vector. These components can be measured (CHRISTENSEN and DRANSFIELD, 2002; DRANSFIELD et al., 2003), but they are rarely surveyed. Usually, they are calculated from the total-field anomaly either in the wavenumber domain (LOURENCO and MORRISON, 1973; PEDERSEN, 1978) or in the space domain through the equivalent-layer technique (DAMPNEY, 1969).

In the case of 2D magnetic bodies, the amplitude of the magnetic anomaly vector is the envelope of both the $x-$ and $z-$components of the magnetic anomaly vector (NABIGHIAN, 1972), regardless of the source magnetization direction. However, in geologic scenarios with 3D magnetic bodies, the amplitude of the magnetic anomaly vector depends on the source magnetization weakly (NABIGHIAN, 1984; HANEY et al., 2003). The weak dependence on the source magnetization direction makes the amplitude of the magnetic anomaly vector an efficient data for interpreting geologic settings with remanently magnetized sources.

In Chapter 3, we follow a non-spectral approach to parametrize the basement through a grid of juxtaposed rectangular prisms, same as in the second chapter.

Differently from the previous non-spectral inversions, we invert the amplitude of the magnetic anomaly vector for simultaneously estimating the depths of the basement relief and the magnetization intensity of the basement rocks. We assume the absence of intrasedimentary igneous intrusions and prior knowledge about the average basement depth. The method requires a uniform magnetization for the basement rocks; however, it does not assume a given magnetization vector. We do not compute the three orthogonal components of the magnetic anomaly produced by prisms through 3D integrals (BHATTACHARYYA, 1964). Rather, we use the fast-forward modeling based on Gauss-Legendre quadrature (GLQ) proposed in Chapter 2 and in HIDALGO-GATO and BARBOSA (2019). Tests on synthetic data and on field data collected over the Foz do Amazonas Basin, Brazil, confirm the potential of the proposed method in retrieving the shape of the basement without specifying the magnetization direction and intensity of the sources.

Chapter 2

Fast 3D magnetic inversion of a surface relief in the space domain

This chapter was published in HIDALGO-GATO and BARBOSA (2019).

2.1 Summary

We present a fast 3D regularized magnetic inversion algorithm for depth-to-basement estimation based on an efficient way to compute the total-field anomaly produced by an arbitrary interface separating nonmagnetic sediments from a magnetic basement. We approximate the basement layer by a grid of 3D vertical prisms juxtaposed in the horizontal directions, where the prisms' tops represent the depths to the magnetic basement. To compute the total-field anomaly produced by the basement relief, the 3D integral of the total-field anomaly of a prism is simplified by a 1D integral along the prism thickness, which in turn is multiplied by the horizontal area of the prism. The 1D integral is calculated numerically using the Gauss-Legendre quadrature produced by dipoles located along the vertical axis passing through the prism center. This new magnetic forward modeling overcomes one of the main drawbacks of the nonlinear inverse problem for estimating the basement depths from magnetic data: the intense computational cost to calculate the total-field anomaly of prisms. The new sensitivity matrix is simpler and computationally faster than the one

using the classical magnetic forward modeling based on the 3D integrals of a set of prisms which parametrizes the earth's subsurface. To speed up the inversion at each iteration, we employ the Gauss-Newton approximation for the Hessian matrix keeping the main diagonal only and adding the first-order Tikhonov regularization function. The large sparseness of the Hessian matrix allows us to construct and solve a linear system iteratively, that is faster and demands less memory than the classical nonlinear inversion with the prism-based modeling using 3D integrals. We successfully inverted the total-field anomaly of a simulated smoothing basement relief with a constant magnetization vector. Test on field data from a portion of the Pará-Maranhão Basin, Brazil, retrieved a first depth-to-basement estimate geologically plausible.

2.2 Forward Model

We assume a sedimentary basin consisting of nonmagnetic sediments overlying a magnetic basement. We adopt the conventional prism-based discretization of the Earth's subsurface for modeling the basement topography from total-field anomaly. We parametrize the basement layer as a grid of M 3D vertical prisms juxtaposed in the horizontal directions of a Cartesian coordinate system, where the $x-$ and $y-$coordinates are, respectively, north and east orientated, the $z-$ coordinate is positive downward. In this discrete model, we assume that the grid encloses all basement topography and the observation grid is co-centered with the basement grid (Figure 2.1). The horizontal dimensions a and b of all prisms are known as shown in Figure 2.1. The depths to the bottoms of all prisms are assumed to be constant z_2, approximately known, and they describe a surface which may coincide with the non-magnetic surface. The depths to the tops of all prisms, $p_j, j = 1, \dots, M$, represent the depths to the basement and are the parameters to be estimated from the total-field anomaly.

We assume that the magnetization vector of each prism is constant. The total-field anomaly calculated at the ith observation point (x_i, y_i, z_i) is given by:

$$\Delta T_i(x_i, y_i, z_i) = \sum_{j=1}^{M} \emptyset_{ij}\,, \qquad i = 1, \dots, N, \tag{2.1}$$

where $\emptyset_{ij}$ is the total-field anomaly produced by the jth prism calculated at the ith observation point with magnetization intensity m, inclination m_i, and declination m_d. The expression of the total-field anomaly produced by the jth prism was derived by BHATTACHARYYA (1964).

Many authors have used equation 2.1 to calculate the total-field anomaly of complex geological layers by discretizing the subsurface with a mesh of M smaller prisms between the top and the bottom of the layer. Nonetheless, the analytical equation of the total-field anomaly produced by a unique prism ($\emptyset_{ij}$) is computationally expensive. On the other hand, the computation of the total-field anomaly produced by a dipole is simpler and, consequently, demands less computational cost. BHATTACHARYA (1964) derived the analytical expression of the total-field anomaly produced by a single prism by integrating the total-field anomaly of a dipole over the volume of the prism, i.e.:

$$\emptyset_{ij}(x_i, y_i, z_i) = \int_{x_{1_j}}^{x_{2_j}} \int_{y_{1_j}}^{y_{2_j}} \int_{p_j}^{z_2} \varphi_{ij}(x', y', z')\, dx' dy' dz', \qquad (2.2)$$

where x_{1_j}, x_{2_j}, $y_{y_{1_j}}$, y_{2_j}, p_j, and z_2 are the horizontal and vertical coordinates of the corners of the jth prism and $\varphi_{ij}(x', y', z')$ is the expression of the total-field anomaly, calculated at the ith observation point, produced by a single jth dipole with magnetic moment having the same direction of the magnetization vector of the prism and located at x', y', and z' denoting, respectively, the $x-$, $y-$, and $z-$coordinates of an arbitrary point belonging to the interior of the jth prism. In equation 2.2, the integration is conducted with respect to the variables x', y', and z'.

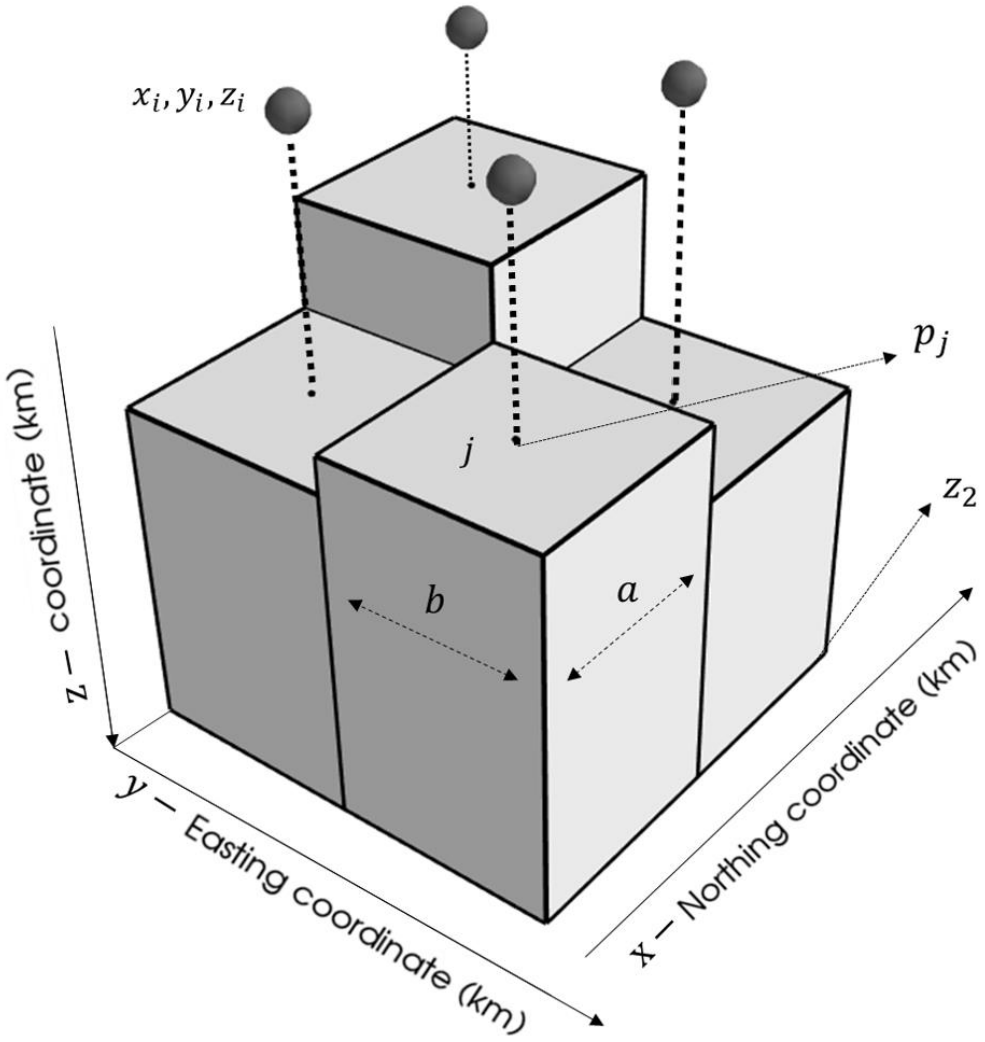

Figure 2. 1: Schematic representation of the interpretative model. The user-specified grid of M 3D vertical prisms encloses all basement topography where the depths to the tops of all prisms, $p_j, j = 1, \dots, M$, represent the unknown depths to the basement. The depths to the bottoms of all prisms are assumed to be constant and known constant bottom.

Integrating equation 2.2 is computationally expensive. Instead, we adopt a simplification which consists in two steps. First, the 3D integral (volume integral) of the total-field anomaly produced by the jth prism (equation 2.2) is simplified by a 1D integral along the jth prism thickness, which in turn is multiplied by the horizontal area (multiplication of the horizontal dimensions a and b of all prisms) of the jth prism, i.e.,

$$\emptyset_{ij}(x_i, y_i, z_i) \approx a.b \int_{p_j}^{z_2} \varphi_{ij}(z')\, dz' , \qquad (2.3)$$

where $\varphi_{ij}(z')$ is the expression of the total-field anomaly, calculated at the ith observation point, produced by a single jth dipole with magnetic moment having the same direction of the magnetization vector of the jth prism and whose horizontal coordinates coincide with the horizontal coordinates of the jth prisms' center. Notice in equation 2.3 that the integration is conducted with respect to the variable z' denoting the $z-$coordinate of an arbitrary point belonging to the interior of the jth prism. In the second step, the 1D integral in equation 2.3 is calculated numerically using the Gauss-Legendre quadrature (GLQ) produced by dipoles located along the vertical axis passing through the center of the jth prism. In the case of GLQ, the one-dimensional integral (equation 2.3) is approximated by a weighted sum of the integration kernel (Abramowitz and Stegun, 1972; see page 887):

$$\int_{p_j}^{z_2} \varphi_{ij}(z')\, dz' \approx \frac{z_2 - p_j}{2} \sum_{i=1}^{n} w_i \quad \varphi_{ij}(z^*{}_i), \qquad (2.4)$$

where n is the quadrature order (number of nodes used in the GQL), $z^*{}_i$, $i = 1, \dots, n$, are the transformed zero-crossings of the nth-order Legendre polynomial $P_n(z')$:

$$z^*{}_i = \frac{z_2 - p_j}{2} z'{}_i + \frac{z_2 + p_j}{2}, \qquad (2.5)$$

where $z'{}_i$ is the ith zero-crossing of $P_n(z')$ and w_i, $i = 1, \dots, n$, are the transformed Gaussian weights computed through linear mapping from unit interval $[-1\ 1]$ to interval $[p_j\ z_2]$ given by:

$$w_i = \frac{2}{\left(1 - z_i'^2\right)\left(P'_n\left(z_i'\right)^2\right)}, \qquad (2.6)$$

where $P'_n(z_i')$ is the first derivative of the nth Legendre polynomial which can be obtained with well-known recursive relations. ABRAMOWITZ and STEGUN (1972) (see page 916) present the zero-crossings $z'{}_i$ and Gaussian weights (equation 2.6) for Gauss-Legendre quadrature up to order 96.

Is well known that the integration accuracy using GLQ depends on the number of dipoles (the number n of nodes) used in the summation (equation 2.4). Actually, the higher order of n produces better approximation of the integral (UIEDA et al., 2016). Hence, the larger the number of dipoles, the better the accuracy of GLQ integration; however, it increases the computational cost. We performe several numerical tests showing that values of n bettween 2 and 4 give a faster solution than the analytical solution of the total-field anomaly produced by a prism (BHATTACHARYA, 1964) with acceptable accuracy. See the Appendix 2.A.

2.3 Inverse Problem

Let $\mathbf{d}^{\mathrm{o}} = [d_1^O, \dots, d_N^O]^T$ be the observed total-field anomaly vector produced by the basement relief of a sedimentary basin. Here, the superscript T indicates transposition. Let $\Delta\mathbf{T}(\mathbf{p}) = [\Delta T_1, \dots, \Delta T_N]^T$ be the predicted total-field anomaly vector (forward model) produced by M prisms that set up the discretization mesh of the basement layer. The ith element of the vector $\Delta\mathbf{T}(\mathbf{p})$ is calculated using the fast-prismatic forward modeling presented in the preceding section using equations 2.1 and 2.3 with GLQ integration (equations 2.4-2.6). Let us assume that the magnetization vector and the depths to the bottom of all prisms z_2 are known. Retrieving the basement depths by estimating the top of each prism ($\mathbf{p} = [p_1, \dots, p_M]^T$) that yields an acceptable observed total-field anomaly fitting is a nonlinear inverse problem. To solve this problem, we minimize the L_2-norm ($\|.\|^2$) of the data-misfit function given by the difference between observed and predicted total-field anomalies, i.e.,

$$\delta(\mathbf{p}) = \|\mathbf{d}^{\mathrm{o}} - \Delta\mathbf{T}(\mathbf{p})\|^2. \tag{2.7}$$

Estimating the parameter vector $\mathbf{p}$ that minimizes the equation 2.7 is an ill-posed inverse problem that needs regularization. We regularize the data-misfit function (equation 2.7) by introducing the smoothness between adjacent parameters, which is also known as first-order Tikhonov regularization (TIKHONOV and ARSENIN, 1977). Hence, we minimize the regularized objective function defined by:

$$\psi(\mathbf{p}) = \delta(\mathbf{p}) + \lambda\|\mathbf{R}\mathbf{p}\|^2, \tag{2.8}$$

where **R** is a first-order finite-difference matrix and λ is a nonnegative scalar that controls the trade-off between the data-misfit function (equation 2.7) and the regularizing function (second term of the right-hand side of equation 2.8). This means that the larger the value of λ, the more stable and smoother are the estimated basement relief but also the larger will be the data-misfit measure.

The solution of equation 2.8 can be found iteratively by using the Gauss-Newton method with the MARQUARDT (1963) strategy (SILVA et al., 2001; SILVA DIAS et al, 2007). Starting with initial depth-to-basement guesses $\widehat{\mathbf{p}}^0$, we estimate, at the kth iteration, a correction vector $\boldsymbol{\Delta}\widehat{\mathbf{p}}^k$ that minimizes the regularized objective function $\psi(\mathbf{p})$ (equation 2.8), i.e.,

$$\boldsymbol{\Delta}\widehat{\mathbf{p}}^{\,k} = \mathbf{H}_k^{-1}\mathbf{J}_k, \tag{2.9}$$

where $\mathbf{H}_k$ and $\mathbf{J}_k$ are, respectively, the Hessian matrix and the gradient vector of the function $\psi(\mathbf{p})$, evaluate at $\mathbf{p} = \widehat{\mathbf{p}}^k$, which are given by:

$$\mathbf{H}_k = \mathbf{A}_k^T\mathbf{A}_k + \lambda\mathbf{R}^T\mathbf{R}, \tag{2.10}$$

and

$$\mathbf{J}_k = \mathbf{A}_k^T\boldsymbol{\varepsilon}^k - \lambda\mathbf{R}^T\mathbf{R}\,\widehat{\mathbf{p}}^k, \tag{2.11}$$

where $\boldsymbol{\varepsilon}^k$ is the difference between observed and predicted total-field anomalies at the kth iteration and $\mathbf{A}_k$ is an N x M sensitivity matrix whose ijth element a_{ij}^k is given by the partial derivative of $\Delta\mathbf{T}(\mathbf{p})$ with respect to the jth parameter calculated at the ith observation point and evaluated at the kth iteration where $\mathbf{p} = \widehat{\mathbf{p}}^k$.

After estimating $\boldsymbol{\Delta}\widehat{\mathbf{p}}^k$ (equation 2.9), we update the depth-to-basement estimates by

$$\widehat{\mathbf{p}}^{k+1} = \widehat{\mathbf{p}}^k + \boldsymbol{\Delta}\widehat{\mathbf{p}}^k. \tag{2.12}$$

This process is repeated until the amplitude of the data-misfit values is below a certain threshold.

2.4 A faster inversion algorithm

Solving equation 2.9 is both time-consuming and memory-costly process because of two main reasons: 1) the need of calculating the forward modeling and the sensitivity matrix at each iteration and 2) the inversion of the Hessian matrix at each iteration.

To tackle the computational hurdle of setting up the sensitivity matrix, we consider our approximation of the forward model given by equations 2.1 and 2.3. Then, the ijth element of the sensitivity matrix $\mathbf{A}_k$, at the kth iteration with $\mathbf{p} = \widehat{\mathbf{p}}^k$, can be written as:

$$a_{ij}^k = \frac{\partial}{\partial p_j}\,\Delta T_i\left(p_j^k\right) \approx \frac{\partial}{\partial p_j}\int_{\hat{p}_j^k}^{z_2} \varphi_{ij}(z')\,dz' \approx -\,\varphi_{ij}\left(\hat{p}_j^k\right). \tag{2.13}$$

Thus, we approximate the ijth element of the sensitivity matrix at the kth iteration by the total-field anomaly produced by the ijth dipole $\varphi_{ij}\left(\hat{p}_j^k\right)$ with horizontal locations x_j' and y_j', vertical location $\hat{p}_j^k$, and magnetic moment computed by multiplying the horizontal area of the prism $(a.b)$ by the magnetization intensity assumed to the basement rocks. Note that the elements of the sensitivity matrix now has an analytical and simple formula (equation 2.13) which is computationally faster than the numerical approximation.

The computational inefficiency of inverting the Hessian matrix (equation 2.9) is due to the large non-sparse matrix $\mathbf{A}_k^T\mathbf{A}_k$ (equation 2.10). To tackle the computational hurdle of inverting the non-sparse Hessian matrix (equation 2.9), we consider only the main diagonal of the sensitivity matrix $\mathbf{A}_k$ whose elements are given by equation 2.13. Hence, the Hessian matrix of the data-misfit function ($\mathbf{A}_k^T\mathbf{A}_k$ in equation 2.10) is replaced by a diagonal matrix $\widetilde{\mathbf{A}}_k$ whose jth diagonal element is given by:

$$\tilde{a}_{jj}^k \approx \varphi_{jj}^2\left(\hat{p}_j^k\right). \tag{2.14}$$

This simplification avoids the inversion of a large non-sparse matrix because the Hessian matrix to be inverted in equation 2.9 is replaced by the sum of sparse matrices given by:

$$\mathbf{H}_k = \widetilde{\mathbf{A}}_k \;+ \lambda\mathbf{R}^T\mathbf{R}. \tag{2.15}$$

By harnessing the sparcity of all matrices that set up the new Hessian matrix (equation 2.15), the computational efficiency to invert this matrix is guaranteed because its inversion demands much less computational cost than equation 2.9.

We stress that the approximation of the sensitivity matrix $\mathbf{A}_k$ by a diagonal matrix is only possible for computing the Hessian matrix (equation 2.15) and not for the gradient. In gravity-data inversions, BOTT (1996), SILVA et al. (2014), and UIEDA and BARBOSA (2017) also used a diagonal matrix to set up the sensitivity matrix to construct both the Hessian matrix and the gradient vector. This is possible because there is a positive correlation between the gravity data and the parameter to be estimated. Rather, in the magnetic-data inversion such correlation does not exist because the magnetization is not a scalar but a vector property, which depends not only on the magnetization intensity but also on the magnetization inclination and declination of the magnetization vector. For this reason, the same approach adopted by BOTT (1996) using gravity data is not possible for magnetic-data inversion due to the dipolar characteristic of the total-field anomaly. Here, the gradient vector $\mathbf{J}_k$ (equation 2.11) is computed by using the full sensitivity matrix $\mathbf{A}_k$ (equation 2.13). And the predicted total-field anomaly is calculated by using the proposed fast-prismatic forward modeling (equations 2.1 and 2.3 with GLQ integration described by equations 2.4-2.6).

Finally, we call attention that our inversion method using fast-prismatic forward modeling (equations 2.1 and 2.3) with GLQ integration (equations 2.4-2.6) and a sparse Hessian matrix (equation 2.15) produces virtually the same result as the classical inversion using the prism-based forward modeling (equations 2.1 and 2.2) and the full Hessian matrix (equation 2.10) with a full sensitivity matrix $\mathbf{A}_k$. This is because we use a conservative number of dipoles (n) from 2 to 4 to guarantee the accuracy of the GLQ integration as we point out in the Appendix A. Moreover, in our inversion method, only the Hessian matrix (equation 2.15) is sparse because it uses a diagonal sensitivity matrix $\widetilde{\mathbf{A}}_k$; however, the gradient vector (equation 2.11) is computed using the full sensitivity matrix and it guarantees the convergence of our nonlinear inversion method.

2.5 Computational-efficiency analysis

Figure 2.2 shows an example of the time required to calculate the forward equation for the classical prism-based forward modeling (equations 2.1 and 2.2) and our proposed fast-prismatic forward modeling (equations 2.1 and 2.3) with GLQ integration (equations 2.4-2.6). We calculate the forward models of a generic basement surface by increasing the number of prisms (number of parameters) from 400 to 2500. In this comparison, we use 4 nodes for the GLQ integration. Both the classical prism-based forward modeling and our approach using equations 2.1 and 2.3 with GLQ integration have $O(N^2)$ dependency with time due to the loop operations. However, the forward model using prisms is computationally more costly than our forward modeling. Figure 2.2 shows the increase in the computational time required for both forward models as the number of prisms increases. By comparing the computational time required for the classical prism-based forward modeling (gray dashed line in Figure 2.2) with our approach using equations 2.1 and 2.3 and the GLQ integration (black solid line in Figure 2.2), we note that our forward modelling has a much better computational efficiency. Specifically, the number of operations for different quadrature orders (n) is of $O(N^2 n)$. Nonetheless, we show that even using a large quadrature order ($n = 4$), the quadrature approximation is faster than the classical prism forward modeling which uses 3D integral. This is mainly due to the number of operations used to calculate the forward model of the prisms $O(8N^2)$ and the complexity of the trigonometric and logarithmic terms inside the prism formulation.

In a classical nonlinear inverse problem, we need to calculate, at each iteration: i) the forward model; ii) the sensitivity matrix and; iii) the Hessian matrix and its inverse. In the inverse problem with the classical prism-based forward modeling (equations 2.1 and 2.2), the sensitivity matrix is calculated by a finite-differences method using two prisms for each ijth element of the matrix. In our proposed inverse method, the elements of the sensitivity matrix are single dipoles (equation 2.13). Thus, for the classical inverse method, the sensitivity-matrix calculation has a number of operations of $O(16N^2)$. Conversely, in our proposed inverse method the elements of the sensitivity matrix are single dipoles (equation 2.13) with a number of operations of $O(N^2)$. We stress that these numbers only indicate the proportional complexity of the number of operations in both processes. Figure 2.2 also shows an example of the time consumption of the inversion using the classical inverse problem based on prism-

based forward modeling (green solid line) and our proposed inverse method (gray solid line). We also note that our inverse method has a much better computational efficiency compared with the classical inverse problem. We stress that the running time differences shown in Figure 2.2 may change due to hardware and different implementation of the algorithms.

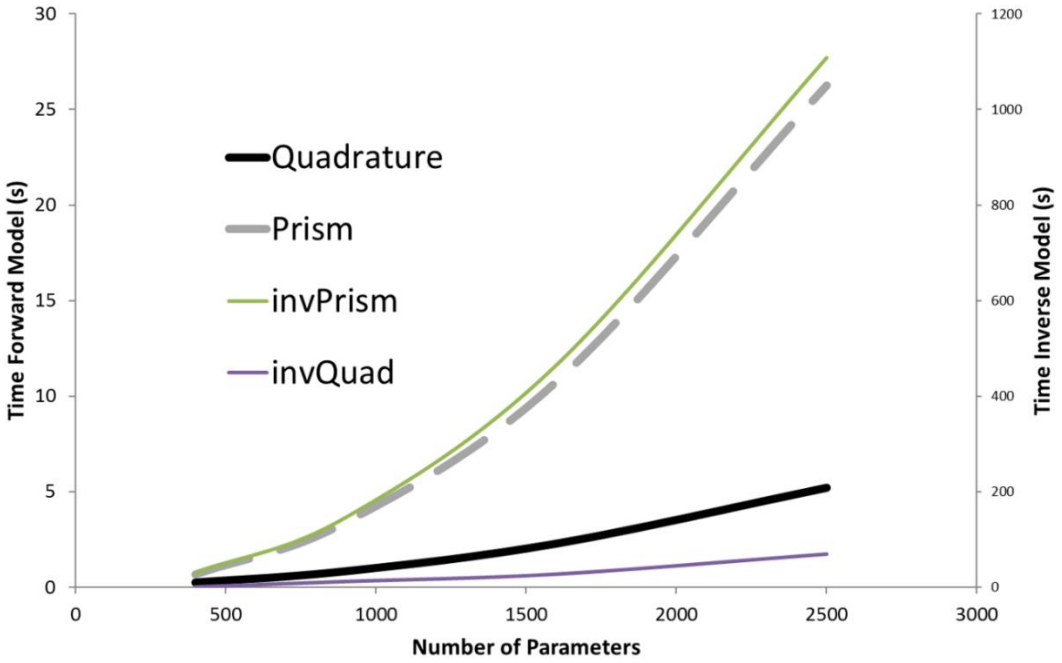

Figure 2. 2: Computational time consumption of the forward modeling using prism (gray dashed curve) and quadrature integral (black solid curve) versus the number of parameters. Computational time consumption of the inversion using prism (green solid curve) and quadrature integral (gray solid curve) versus the number of parameters.

2.6 Determining the magnetization direction

The magnetization vector of the basement layer is a hyperparameter of the inversion because the depth-to-basement estimates are influenced by this vector; but it is not directly estimated in the inversion. Here, we assume a constant magnetization vector for the entire basement with known magnetization intensity but unknown magnetization direction (inclination m_i and declination m_d). Hence, to estimate the basement relief, we first need to determine the basement's magnetization direction.

Several authors have presented different methodologies to estimate the magnetization direction of isolated sources (e.g., FEDI et al., 1994; MEDEIROS and SILVA, 1995; PHILLIPS, 2005; DANNEMILLER and LI, 2006; NUNES et al., 2008; GEROVSKA et al., 2009; OLIVEIRA Jr. et al., 2015). Here, we adapt a methodology proposed by NUNES et al. (2008) to determine the magnetization direction.

To determine the optimum pair of inclination $m_i^* \in [-50°, 50°]$ and declination $m_d^* \in [-180°, 180°]$ of the magnetization vector of the basement layer, we assume a uniformly magnetized basement with known magnetization intensity. We determine the optimum pair $(m_i^*,\ m_d^*)$ in the following way. We fix a pair of values of m_i and m_d and estimate the basement depths $\widehat{\mathbf{p}}$ that minimize the regularized objective function ($\psi(\mathbf{p})$, equation 2.8). Next, we plot the data-misfit function ($\delta(\mathbf{p})$, equation 2.7) on the plane $m_i \times m_d$. This procedure is repeated for different pairs of m_i and m_d to produce a discrete mapping of $\delta(\mathbf{p})$ on the plane $m_i \times m_d$ for a given increment of m_i and m_d. After drawing the discrete mapping of $\delta(\mathbf{p})$ on the plane $m_i \times m_d$, with m_i varying from $-50°$ to $50°$ and m_d varying from $-180°$ to $180°$, the optimum pair $(m_i^*,\ m_d{}^*)$ is the one that produces the smallest value of $\delta(\mathbf{p})$.

2.7 Application to synthetic data

Figure 2.3a shows the noise-corrupted total-field anomaly produced by a simulated 3D basement relief of a sedimentary basin (Figures 2.4a and 2.4b). The geological layer between the top of the basement (Figures 2.4a and 2.4b) and the bottom of a flat surface (non-magnetic surface at 8 km deep) was discretized by $10{,}000$ juxtaposed vertical prisms with constant magnetization of 2.0 A/m and inclination and declination, equal to $45°$ and $20°$, respectively, in the same direction of the geomagnetic field. All the geological sources located between the basement relief and the Earth's surface are nonmagnetic sediments.

The depth of the basement varies from 418 m to 4375 m in an area of ~256 km^2 with a single depocenter elongated in the northwest-southeast direction (Figure 2.4b). By using the implementation of UIEDA et al. (2013), we calculate the total-field anomaly produced by the prismatic bodies at an elevation of 150 m on a regular grid of 100 × 100 observation points with a horizontal resolution of 160 m. The anomaly

is corrupted with pseudorandom zero-mean Gaussian noise with a standard deviation of 10 nT (Figure 2.3a).

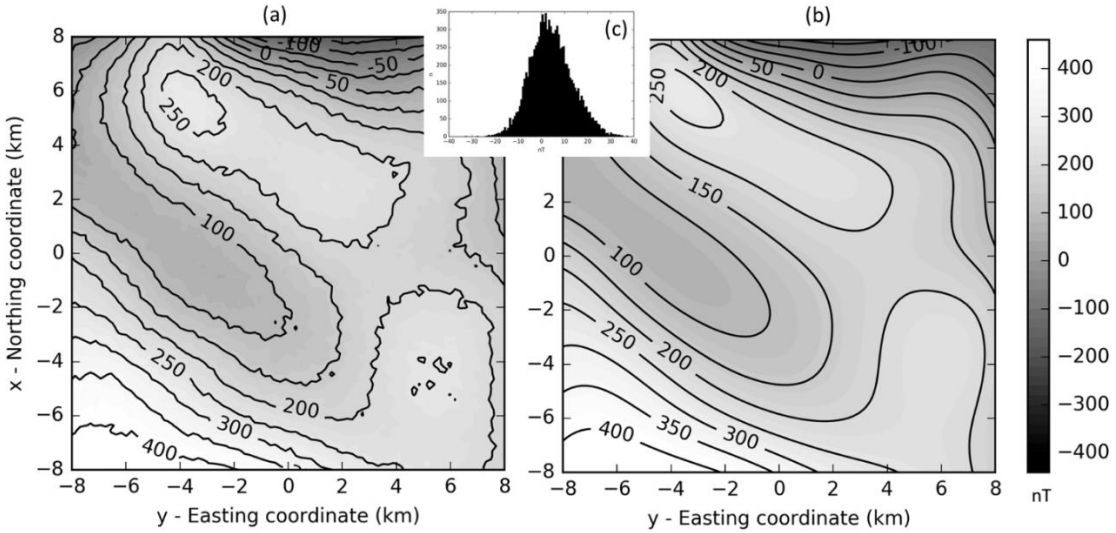

Figure 2. 3: Noise-corrupted (a) and predicted (b) total-field anomalies; the former is produced by the simulated basement relief shown in Figure 2.4 and the latter is produced by the corresponding estimated basement relief shown in Figure 2.5. The histogram distribution (c) shows the differences between observed and predicted data.

To minimize the edge effects, we extend both the interpretation model and the observed data beyond the easternmost, westernmost, northernmost, and southernmost limits of the observed data. This extension extends 20% beyond the edges of the observed data. We invert the extended observation grid (Fig 2.3a) to recover the basement relief of the simulated sedimentary basin (Fig 2.4a and 2.4b) using our method and assuming the magnetization vector direction and intensity is known. The predicted total-field anomaly is computed by our fast-prismatic forward modeling using equations 2.1 and 2.3 with the GLQ integration with a number of nodes $n = 2$ as described before. We also test $n = 3$ and 4; however, the differences between the calculated total-field anomaly with the GLQ method are lower than 1%. Thus, the weighted sum of two dipoles located along the $z-$axis of each prism is sufficient to approximate the total-field anomaly produced by a 100×100 grid of 3D vertical juxtaposed prisms in both horizontal directions. Our iterative inversion runs over 18 iterations using $\lambda = 0.0001$, which was determined using the standard L-curve approach (HANSEN, 1992). The starting guess to the basement depths $\widehat{\mathbf{p}}^0$ is a vector with all elements equal to 3 km.

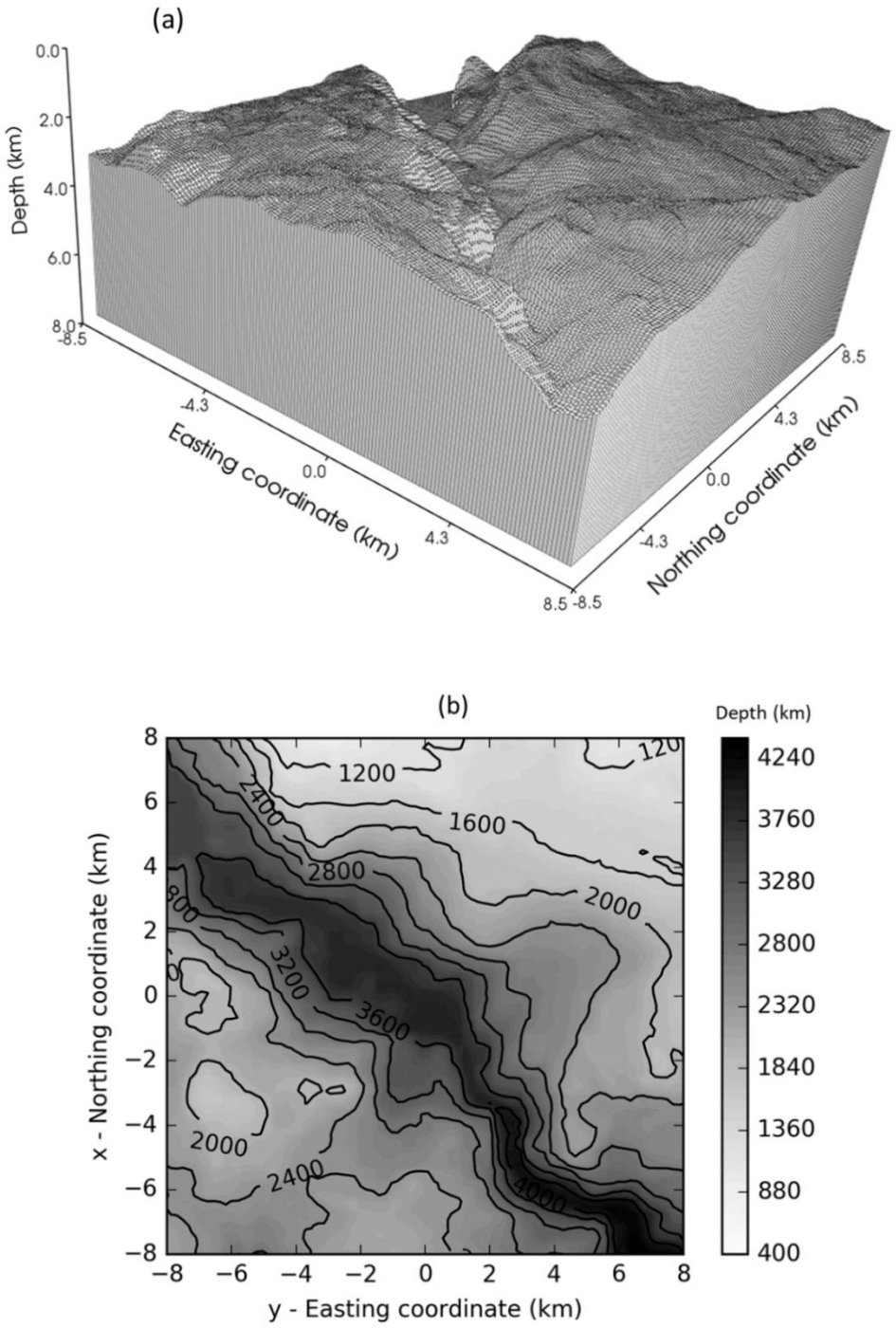

Figure 2. 4: Perspective view (a) and contour map (b) of the simulated basement relief.

Figure 2.3b and 2.3c shows, respectively, the predicted total-field anomaly produced by the depth-to-basement estimates shown in Figure 2.5b and the histogram of the inversion residuals (observed minus predicted data). As we can see, the predicted total-field anomaly (Fig 2.3b) adjusts the observed data (Fig 2.3a) with the histogram of residuals resembling a Gaussian distribution with zero mean and standard deviation of ± 10 nT (Fig 2.3c). The estimated basement relief (Fig 2.5b) has

predominately lower wavenumber spectral contents than the simulated basement (Fig 2.5a and 2.6), which is dominated by both low- and high-wavenumber features.

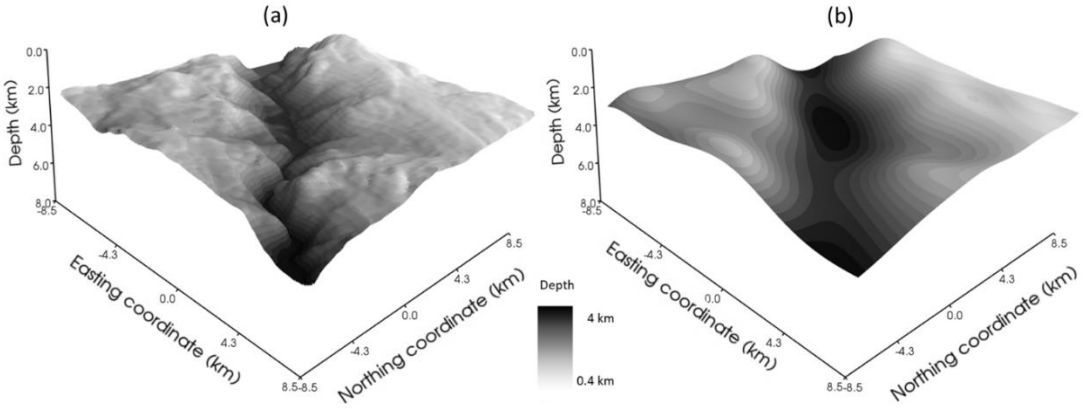

Figure 2. 5: Perspective views of the simulated (a) and estimated (b) basement reliefs.

Our method is not able to recover the high-wavenumber features of the simulated basement relief because the observed magnetic data does not reflect such steep variations. Figure 2.6 shows a vertical cross-section along a profile in the east-west direction at $x = 0$ where the tops of the prisms describe the simulated basement relief and the black solid line is the estimated basement relief. We note in this profile that the smoothness of the estimated basement relief is evident.

We perform a numerical analysis to investigate the sensitivity of our method to the use of different initial guesses. Here, the results of this analysis are displayed along a profile (Fig 2.6); however, this analysis is performed using a grid of data. Figure 2.6 shows a vertical cross-section along a profile in the east-west direction at $x = 0$ where the tops of the prisms describe the simulated basement relief. The blue, red, black, and green solid lines are the estimated basement reliefs obtained with four different initial guesses to the basement depths which are planar surfaces at 4, 3, 2 and 1 km deep. We call to attention that even setting different surfaces as initial guesses, our method retrieves magnetic basement reliefs (coloured lines in Figure 2.6) close to each other. Moreover, the most striking feature in Figure 2.6 that deserves our attention is that the initial guess does not need to be an average of the depths of the true magnetic basement relief. This sensitivity analysis shows the robustness of our method to the choice of the initial guess that can be a planar surface at any depth. We stress that the sensitivity of our method to uncertainties in the magnetization contrast of the magnetic basement (not shown) is trivial. By assigning a magnetization contrast smaller than the

true one, the estimated basement relief is deeper when compared with the true one. Conversely, by assigning a magnetization contrast larger than the true one, the estimated basement relief is shallower than the true one.

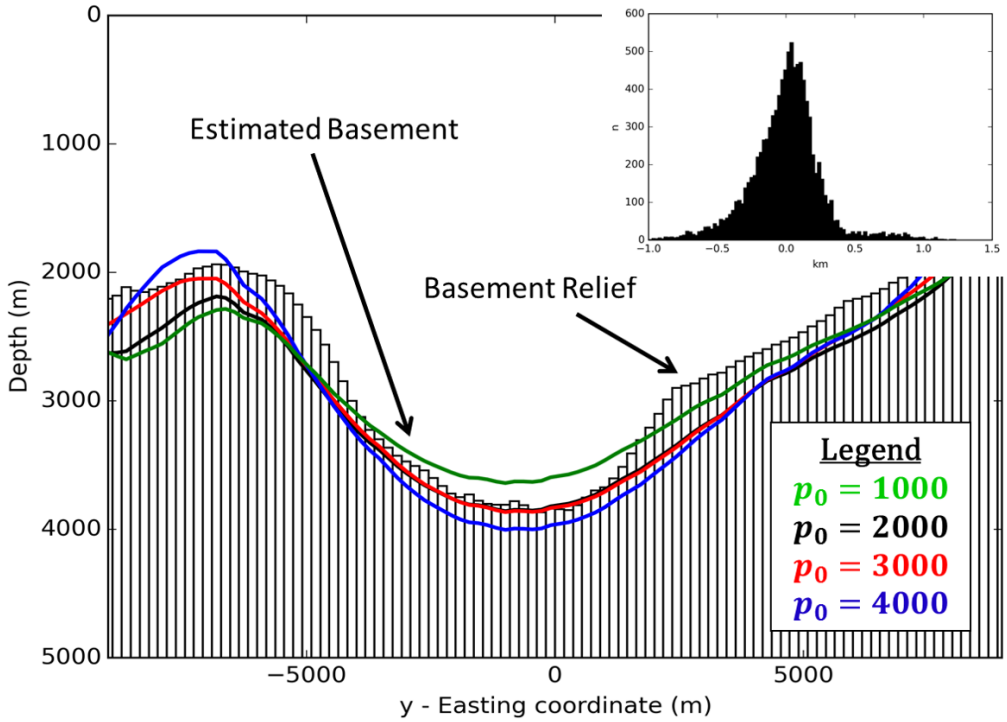

Figure 2. 6: East-West profile at the constant x −coordinate at zero showing the simulated basement (top of the prisms). The blue, red, black, and green solid lines are the estimated basement reliefs obtained with four different initial guesses to the basement depths, which are planar surfaces at 4 km, 3 km, 2 km, and 1 km deep, respectively. The histogram distribution shown as an inset of the differences between simulated and estimated basement depths along the profile using a planar surface at 3 km as the initial guess.

In Appendix 3.A we show a synthetic test at induced low latitudes. We simulated a sequence of horst and grabens and inverted the total-field anomaly to recover the simulated basement relief.

2.8 Geological background and magnetic data from Pará-Maranhão Basin

We applied our method to the total-field anomaly from the Pará-Maranhão Basin, located in the Brazilian equatorial margin. The Brazilian equatorial-margin basins are characterized by their northwest-southeast en-echelon trend. The tectonic evolution of the Brazilian equatorial margin is linked to the oblique opening of the Equatorial Atlantic Ocean after the Gondwana breakup.

The Pará-Maranhão is an offshore basin located between the Foz do Amazonas Basin to the northwest and the Barreirinhas Basin to the southeast as shown in Figure 2.7 (modified from HIDALGO-GATO and BARBOSA, 2015). The basement of the Pará-Maranhão Basin is mainly formed by the São Luis Craton, which is a fragment of the West African Craton that was broken during the Atlantic rifting process and the consequent opening of the Atlantic Ocean. HIDALGO-GATO and BARBOSA (2015) show a structural map with several transition zones corroborated using the local phase in the scale-space monogenic signal. The study area is located at the northwest portion of the Pará-Maranhão Basin, extending from the shallow basement to deep waters where the transition between continental and oceanic crusts occurs. There are no evidences of igneous intrusions on this portion of the basin. Hence, it is reasonable to consider nonmagnetic sediments in this study area.

The magnetic data is a public airborne survey flown in 2003 at a height of 150 m. The averages of the inclination and the declination of the geomagnetic field at the acquisition date are $-2°$ and $-20°$, respectively. The data were gridded at a constant observation surface $z = -150\,m$. Figure 2.8a shows the total-field anomaly on a regular grid of 100 by 100 observation points regularly spaced at 1.5 km in both north-south and east-west directions. The total-field anomaly measures were mostly positive (not shown), which is an unexpected behaviour. Hence, we removed a regional component from the total-field anomaly data consisting of a constant average value (not shown).

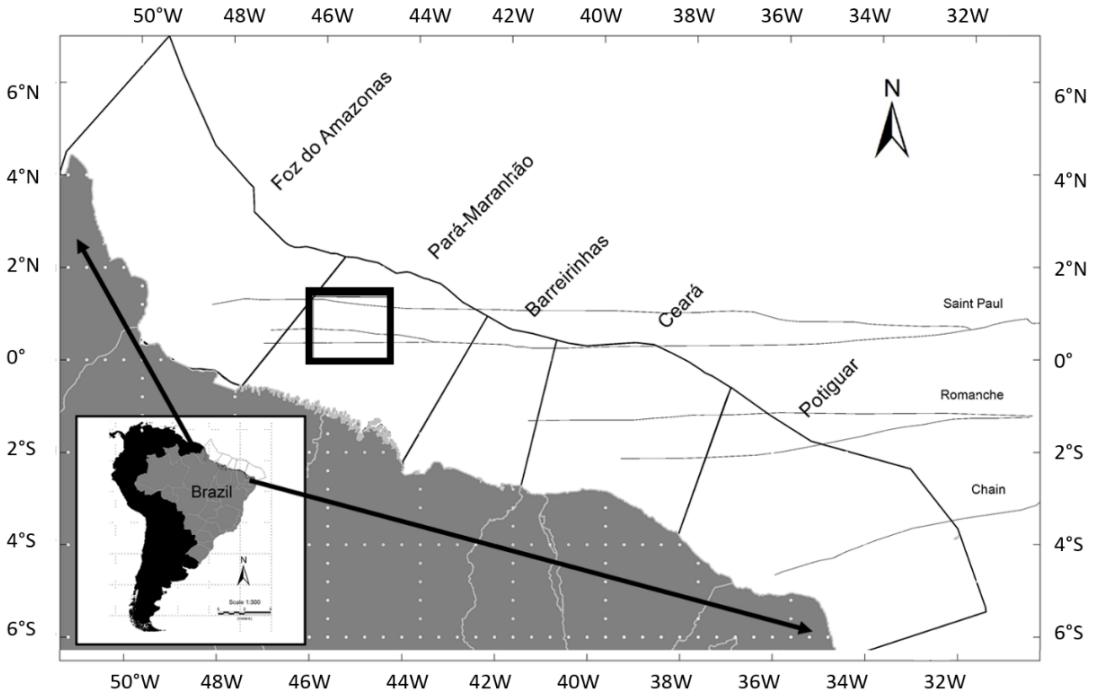

Figure 2.7: Location of the Pará-Maranhão Basin (Brazil) (Modified from HIDALGO-GATO and BARBOSA, 2015) and the study area (black square).

2.9 Real Data: Depth-to-basement estimates

We assume a constant magnetization vector for the entire basement of the study area with a known magnetization intensity of 4.0 A/m grounded on the basement rocks and unknown magnetization direction. To determine an optimum inclination and declination of the magnetized basement, we perform the inversion on a coarse grid of 45 × 37 observation points in the north-south and east-west directions. We produce a discrete mapping of the data-misfit function ($\delta(\mathbf{p})$, equation 2.7) on the domain of $m_i \times m_d$ considering an interval of inclinations varying from -50° to 50° and an interval of declinations varying from -180° to 180° of the magnetization vector of the basement. Figure 2.10 shows the mapping of $\delta(\mathbf{p})$ in logarithmic scale with a step of 5° for both m_i and m_d in Cartesian coordinates (Figure 2.10a) and in polar coordinates (Figure 2.10b).

Note that two well-defined minima of the data-misfit measure (pinpointed as stars in Figure 2.10a and 2.10b) are achieved when the magnetization vector of the basement has an inclination close to $-10°$ and a declination around 160° and when the

magnetization vector has an inclination of $-5°$ and a declination of $-20°$. Because the latter magnetization vector of the basement is close to the magnetization vector of the geomagnetic field (inclination of $-2°$ and declination of $-20°$) and considering that the discrete mapping was set up with increment of 5° for both m_i and m_d, we assumed an induced magnetization of the basement; i.e., the magnetization vector of the basement is equal to the geomagnetic field.

Because we have two well-defined minima of the data-misfit measure (Figure 2.10), two hypotheses of magnetization directions will be used to estimate two versions of the magnetized basement relief. The first inversion considers only induced magnetization (inclination of $-2°$ and declination of $-20°$) while the second inversion considers the hypothesis of remanent magnetization vector with an inclination of $-10°$ and a declination of 160°. To minimize the undesirable edge effects in the estimated basement relief, we extended the interpretation model area horizontally by 20% of the total area and introduced the effect generated by this extension into the observed total-field anomaly data.

To estimate the basement depth by inverting the observed total-field anomaly (Figures 2.8a and 2.9a), we adopt the following tests:

1) In the first test, the magnetization vector of the basement is considered constant in the direction of the geomagnetic field. Hence, an induced magnetization with an intensity of 4.0 A/m for the entire magnetized basement is only considered. We use an initial guess of the basement depths $\widehat{\mathbf{p}}^0$ as a 6 km-deep flat surface. To calculate the predicted total-field anomaly (equations 2.1 and 2.3), we use the GLQ integration with a number of nodes $n = 4$. Our inversion algorithm reaches a satisfactory data-misfit value after 3 iterations using $\lambda = 0.001$. Figure 2.8b shows the predicted total-field anomaly produced by the estimated basement relief shown in Figures 2.11a. As we can see, the histogram of the residuals (Fig 2.8c) corroborates the acceptance of the data fitting.
2) In the second test, the magnetization vector of the basement is considered constant with inclination of $-10°$ and a declination of 160°. Hence, a remanent magnetization vector with an intensity of 4.0 A/m is considered. We also use an initial guess of the basement depths $\widehat{\mathbf{p}}^0$ as a 6 km-deep flat

surface. To calculate the predicted total-field anomaly (equations 2.1 and 2.3), we use the GLQ integration with a number of nodes $n = 4$. Our inversion algorithm reaches a satisfactory data-misfit value after 3 iterations using $\lambda = 0.001$ (the same as test 1). Figure 2.9b shows the predicted total-field anomaly produced by the estimated basement relief shown in Figures 2.11b. Note that the histograms distribution (Figure 2.9c) shows less residuals than the inversion considering only induced magnetization (Figure 2.8c).

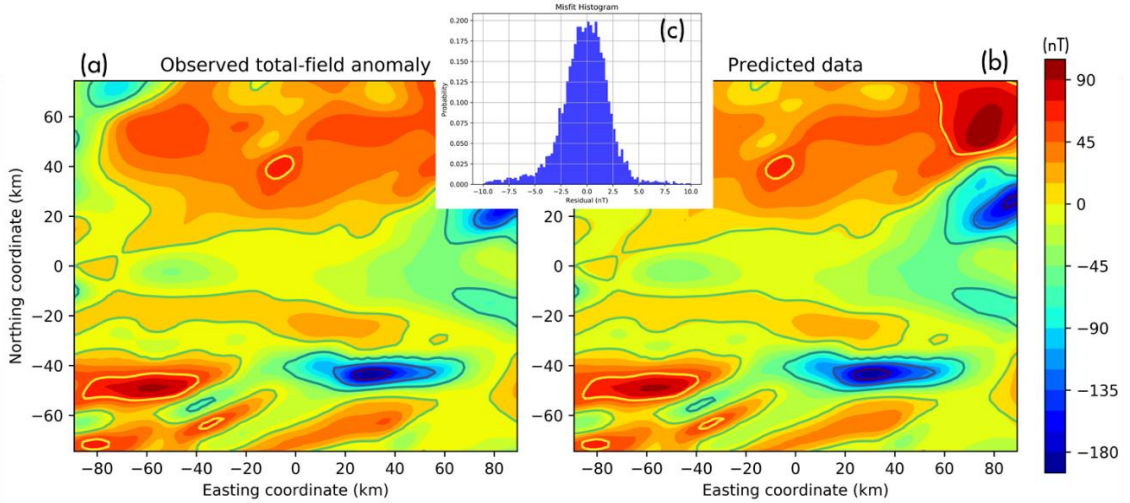

Figure 2.8: Real case study – Under the hypothesis of induced magnetization with inclination $-2°$ and declination -20°. Observed (a) and predicted (b) total-field anomalies; the latter is produced by the estimated magnetic basement relief shown in Figure 2.11a. The histogram distribution (c) shows the differences between observed (a) and predicted (b) data.

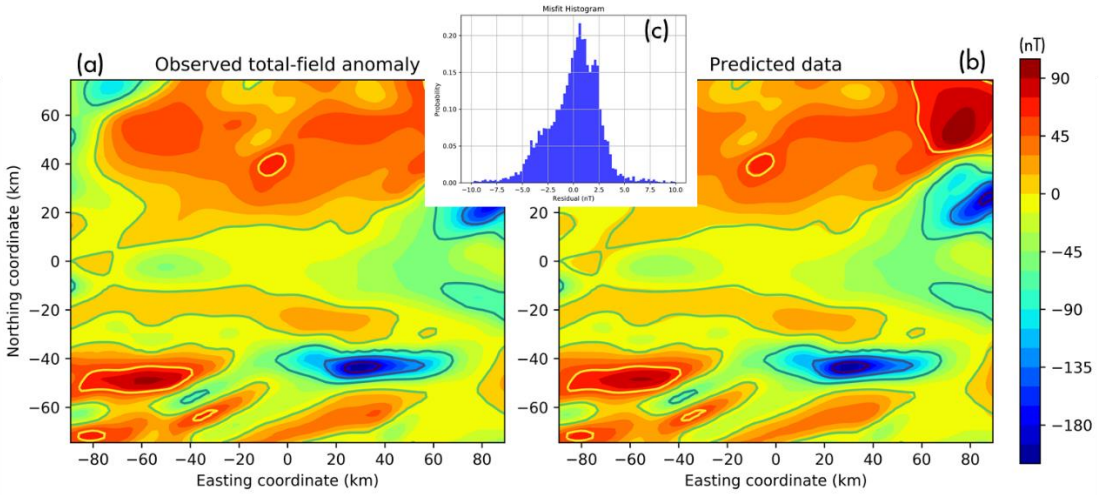

Figure 2.9: Real case study – Under the hypothesis of remanent magnetization with inclination 2° and declination 160°. Observed (a) and predicted (b) total-field anomalies; the latter is produced by the estimated magnetic basement relief shown in Figure 2.11b. The histogram distribution (c) shows the differences between observed (a) and predicted (b) data.

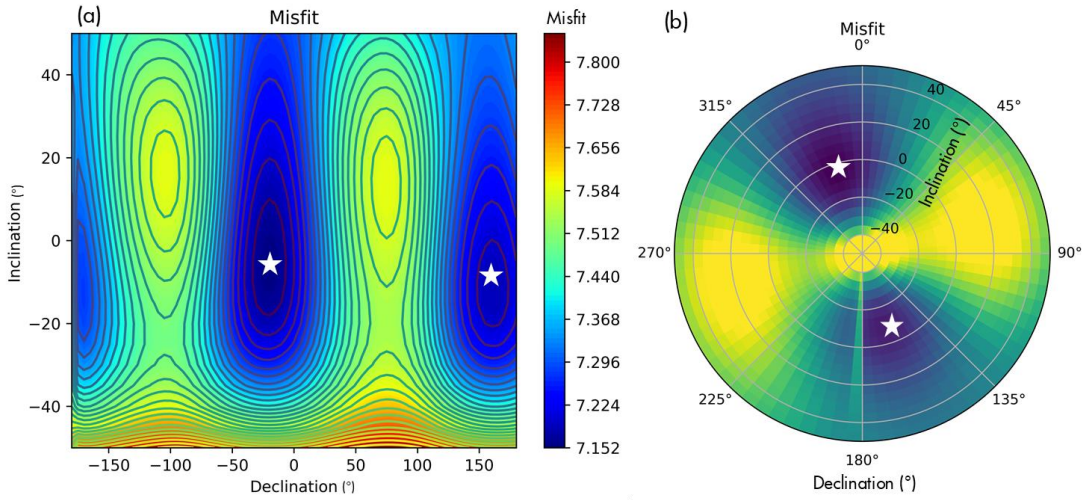

Figure 2.10: Contour maps of the logaritmic data-misfit function (log $(\delta(\mathbf{p}))$, equation 2.7) on the plane $m_i \times m_d$ using a step of 5° for both m_i and m_d in Cartesian coordinates (a) and polar coordinates (b). The white stars pinpoint two optimum pairs of the inclination and declination of the magnetized basement of the study area.

The depth-to-basement estimate using an induced magnetization vector (Figure 2.11a) shows an expected north-eastward crustal thinning as we move from the shore to the continent-ocean-boundary. The northernmost portion of the estimated basement

shows an abrupt increase of depths (maximum of 7 km). We note that in the northern portion, the continental-oceanic boundary probably appears as a deep basement depth with crustal thinning. On the other hand, the depth-to-basement estimate using a remanent magnetization vector shown in Figure 2.11b shows an uplift of the basement to the northern portion of the area. Ergo, the estimated basements (Fig 2.11a and 2.11b) shows an opposite shape as expected. An east-west elongated basement trend is observed between the two southward branches of the Saint Paul transfer zone in both basement surfaces (Fig 2.11a and 2.11b). There is an ambiguity in the magnetization direction as shown in Figures 2.10a and 2.10b. Given the geological framework of this part of the basin (ZALAN, 2017), we believe that the most likely basement surface is the one produced by the inversion test 1 (Fig 2.11a) with the hypothesis of induced magnetization only.

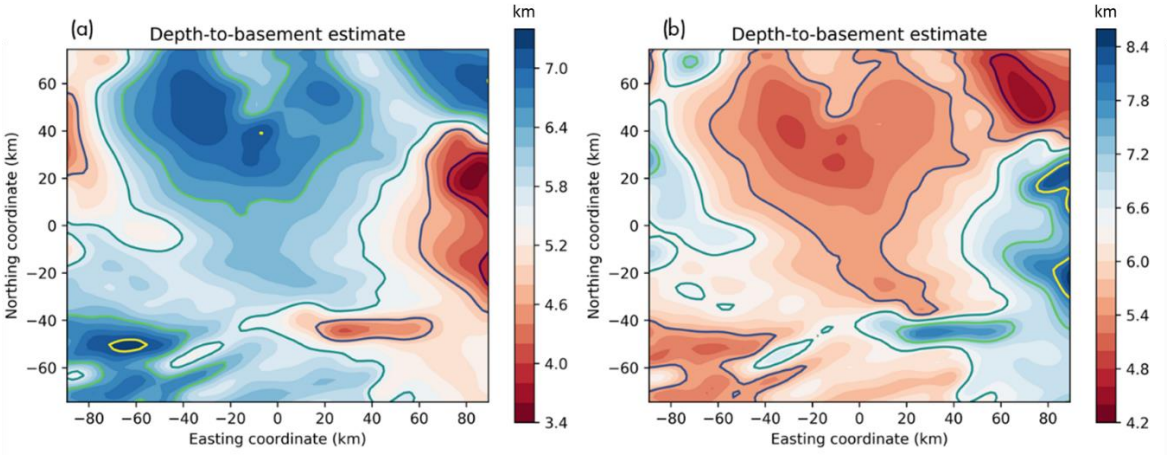

Figure 2.11: Contour maps of the estimated depths of the basement surfaces considering induced magnetization (a) and remanent magnetization vector (b).

In appendix 2.B, we apply this workflow to a synthetic test with magnetization direction at low latitude.

2.10 Final considerations

We have developed a regularized nonlinear total-field anomaly inversion to estimate the depths of the magnetic basement of a sedimentary basin with nonmagnetic sediments and without intra-sedimentary igneous intrusions. We approximated the basement layer by a grid of 3D vertical prisms juxtaposed in the horizontal directions of a right-handed coordinate system. The depths to the tops of the prisms approximate the depths to the basement relief in a discrete way and they are the unknown parameters to be estimated. The computational efficiency of our inversion method is higher because we used an efficient way to compute the forward modeling of the magnetic data of a prism. First, the volume integral of the magnetic data of a prism is simplified by a 1D integration taken with respect to the z-axis of a prism (prism thickness). Then, the 1D integral over the prism thickness is multiplied by the horizontal area of the prism. Finally, the 1D integral of magnetic data of a prism is solved numerically using the Gauss-Legendre quadrature yielded by weighted sums of dipoles effects located along the z-axis of the prism passing through the prism center.

The computation time of our method is also speeded up by replacing the full sensitivity matrix by the magnetic response produced by a single dipole located at the top of each prism. Additionally, we employed the Gauss-Newton approximation for the Hessian matrix maintaining the main diagonal only and adding the first-order Tikhonov regularization function. We stress that the gradient vector in the Gauss-Newton optimization problem is calculated by using the full sensitivity matrix. The numerical studies showed that our magnetic inversion to estimate the depths to the basement is faster than the standard volume-integration method to calculate the magnetic response of a set of prisms.

Because our magnetic inversion method requires the magnetization vector direction to be known, we assumed a uniformly magnetized basement with known magnetization intensity and determined the magnetization direction (inclination and declination). The knowledge about the magnetization intensity could be provided by the information on the basement rocks. For determining the inclination (m_i) and declination (m_d) of the magnetization vector of the basement layer, we constructed a discrete mapping of the data-misfit function on a plane $m_i \times m_d$. The best pair (m_i,m_d) is the one that yields the minimum of the mapped data-misfit function.

We applied our inversion algorithm to a complex synthetic data. Our tests showed the robustness of our method to the choice of the initial guess that could be a surface at any depth. Hence, the interpreter does not need to know an average of the depths of the true magnetic basement relief. However, our method is sensitive to the dipole moment (the product of magnetization intensity multiplied by volume); hence, this is a limitation because it requires the prior knowledge of the magnetization intensity of the basement, which in turn can be provided by the knowledge of the basement rocks. We evaluated the performance of our method by applying it to a real magnetic data from the Pará-Maranhão Basin, offshore northern Brazil. The discrete mapping of the data-misfit function on a plane $m_i \times m_d$ for intervals of $m_i \in [-50°, 50°]$ and $m_d \in [-180°, 180°]$ shows two minima. Hence, we tested two hypotheses of the direction of the magnetization vector to estimate the basement relief of the Pará-Maranhão Basin: (1) induced magnetization vector, and (2) remanent magnetization vector. The depth-to-basement estimate using an induced magnetization vector yields an acceptable data fitting and shows an expected north-eastward crustal thinning as we move from the shore to the continent-ocean-boundary.

We stress that the depths-to-basement estimates, both in the synthetic and in field data, are not able to retrieve the shortest wavelength feature in the basement due to the imposed smoothness constraint by the first-order Tikhonov regularization, which tends to smooth sharp variations in the solution.

Our magnetic inversion could be easily adapted to the gravity inversion by substituting the dipole field by a point of mass. The extension of our magnetic inversion to other types of regularization (e.g., total variation) and misfit functions (e.g., L_1-norm of the data-misfit function) has no methodological hindrances. Finally, our work can be extended to deal with a horizontally varying magnetization vector as long as the horizontal-varying magnetization intensity and the horizontally varying magnetization direction be known such as in Parker's forward modelling. Moreover, in real-data application, we can invert a small piece of the data if the total magnetic vector is known.

2.11 Appendix 2.A: Accuracy Analysis of The Fast-Prismatic Forward Modeling

The key controlling point of the integration accuracy using GLQ depends on the number of dipoles n (equation 2.4). Specifically, n controls not only the accuracy of the numerical integration but also the computation time. The larger the number of dipoles, the better the accuracy of the GLQ integration, but also the higher the computational cost. Here, we investigate how many dipoles (n) are necessary to obtain a faster and more accurate total-field anomaly produced by our forward modeling (equations 2.1 and 2.3) with GLQ integration (equations 2.4-2.6). The reference against which we compare our proposed forward modeling is the analitycal solution of the total-field anomaly produced by the classical prism-based forward modeling (equations 2.1 and 2.2).

The choice of n depends on the thickness of the prism (t) versus the distance between the top of the prism (basement depth) to the observation point (h). We have determined optimal number of dipoles (n) for the total-field anomaly by comparing the computed prism effect proposed in this work (equations 2.1 and 2.3) using GLQ integration (equations 2.4-2.6) with one of the classical prism analytical expression proposed by BHATTACHARYA (1964) (equations 2.1 and 2.2). The metric chosen to evaluate the optimal number of dipoles based on the accuracy analysis is the normalized root mean square between the two total-field anomalies, i.e.,

$$NRMS = 1 - \frac{RMS(\Delta\mathbf{T} - \Delta\mathbf{T_B})}{RMS(\Delta\mathbf{T}) + RMS(\Delta\mathbf{T_B})}, \qquad (2.A\text{-}1)$$

where $\Delta\mathbf{T}$ and $\Delta\mathbf{T_B}$ are N-dimensional total-field anomaly vectors produced by the fast-prismatic forward modeling presented in this work (equations 2.1 and 2.3 using GLQ integration through equations 2.4-2.6) and by the prism-based forward modeling (equations 2.1 and 2.2) proposed by Bhattacharya (1964). In equation 2.A-1, $RMS(.)$ is the root mean square of a vector. Here, the values of $NRMS$ (equation 2.A-1) are limited to the range 0-1. If both data ($\Delta\mathbf{T}$ and $\Delta\mathbf{T_B}$) are close to each other the $NRMS$ is close to one, and thus, the best acurracy of our fast-prismatic forward modeling ($\Delta\mathbf{T}$) is guaranteed.

To perform the accuracy evaluation of the proposed fast-prismatic forward modeling, we simulate a single 3D prism with horizotal dimensions of 50 m and center

located at 0 km in both north-south and east-west directions. The prism is uniformly magnetized by induction only, with a magnetization intensity of 10 A/m and inclination of 45°, declination of -20°. The noise-free total-field anomalies ($\Delta\mathbf{T}$ and $\Delta\mathbf{T}_{\boldsymbol{B}}$) are computed on a plane surface at the nodes of a 20 x 20 grid with a grid spacing of 500 m in both north-south and east-west directions. The thickness of the prism (t) varies from 0 to 20 km (the x-axes in Fig 2.12). The distance between the top of the prism and the plane observation surface (h) varies from 0 to 15 km (the y-axes in Figure 2.12). In this simulation, the depth to the top of the prism starts from 100 m.

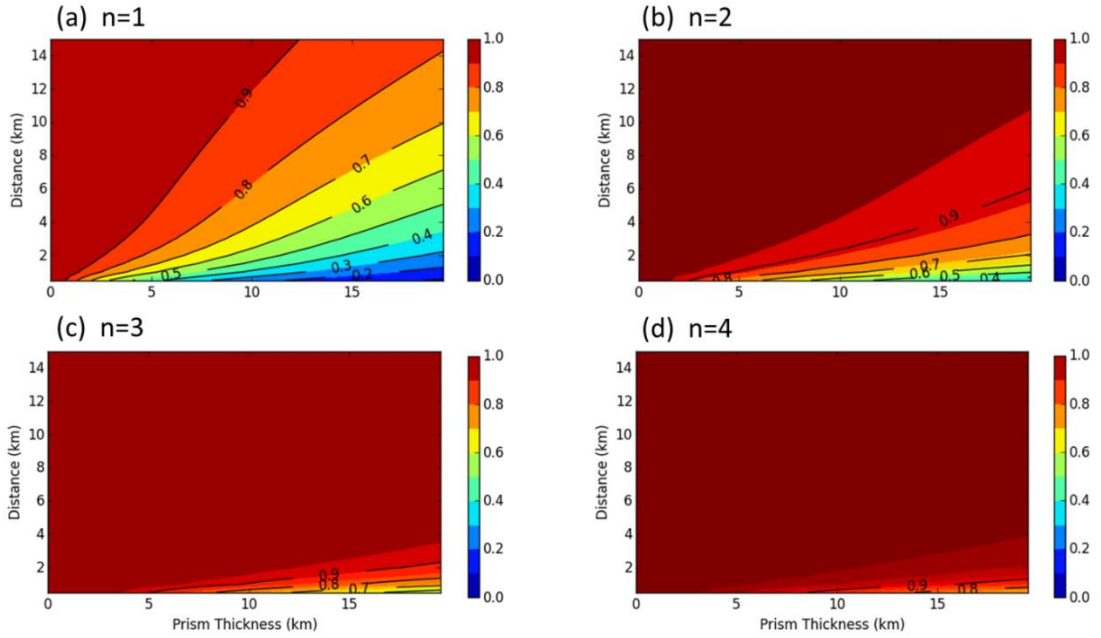

Figure 2.12: Results from the accuracy analysis of the fast-prismatic forward modelling. Contour maps of $NRMS$, on plane $t \times h$, (equation 2.A-1) with number of dipoles of (a) n = 1, (b) n = 2, (c) n = 3 and (d) n = 4. Here, t is the thickness of the prism and h is the distance between the top of the prism and the observation, The dark-red-filled contour intervals produce an accurate computation of the total-field anomaly by the proposed fast-prismatic forward modelling (equations 2.1 and 2.3 using GLQ integration through equations 2.4-2.6) comparing with the prism-based forward modelling (BHATTACHARYA, 1964).

Figure 2.12 a-d shows the map of $NRMS$, on plane $t \times h$, with the number of dipoles n varing from 1 to 4, respectively. The acceptable accuracy of the proposed fast-prismatic forward modeling (equations 2.1 and 2.3 using GLQ integration through equations 2.4-2.6) in comparison with the prism-based forward modeling (BHATTACHARYA, 1964) lies inside the dark-red-filled contour intervals (Fig 2.A-

1) where the $NRMS$ is close to one. All pairs (t and h) that lie inside the dark-red regions in Figure 2.A-1 yield an accurate computation of the total-field anomaly by our fast-prismatic forward modeling. Based on these tests, the best trade-off between accuracy and computation time is when the number of dipoles n varies from 2 to 4. This range of n is addopted here as a conservative choice to compute the total-field anomaly.

Another key sensitivy parameter in the GLQ method is the size of the prism related to the observation distance. As expected, a 1D integral over a 3D volume could only be valid if the horizontal area of the prism is significantly smaller than the distance between the observation heigh and the depth of the prisms. To perform this accuracy evaluation, we simulate a single 3D prism uniformly magnetized by induction only, with a magnetization intensity of 4 A/m and inclination of 45° and a declination of -20°. The prism is located at the center of the grid. The size of the grid, hence the size of the prism, was varied together with the obsevartion distance. We calculated the noise-free total-field anomalies ($\Delta\mathbf{T}$ and $\Delta\mathbf{T}_{\boldsymbol{B}}$) produced by each pairs; prism size vs observation depth to calculated the *NRMS* guiven by equation 2.A-1. Figure 2.13 shows the mapped *NRMS* of the sensibility test by changing the thickness of the prism from 1 km to 10 km and the observation depth from 1 km to 11 km. Note that, for observations distances grather than the size of the prism, the error of the quadrature approximation is less than 10%. (white dashed line). We higlhy recommend using this criteria in the GLQ method.

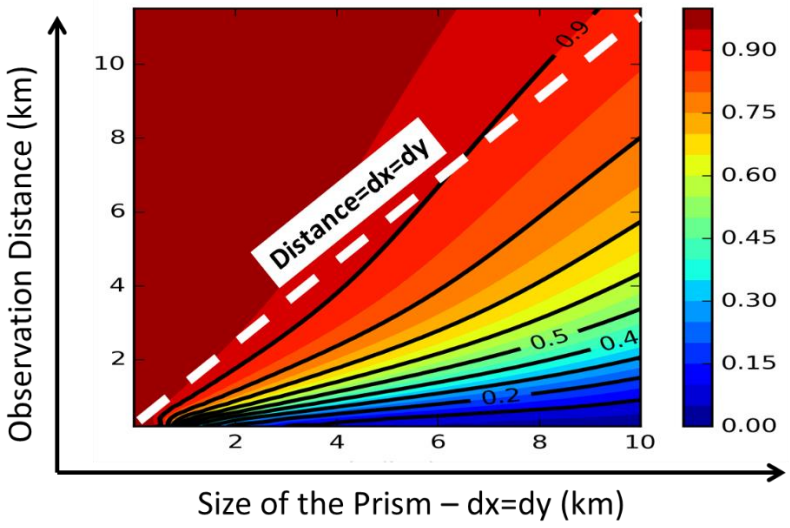

Figure 2.13: Results from the accuracy analysis of the prism size with the observation depth. The white dash line divides the areas were the accuracy level is above acceptable values.

2.12 Appendix 2.B: Magnetization direction estimating using the proposed search workflow

Here, we apply to synthetic data the same workflow used in the real-case study (sections 2.8 and 2.9). In this way, we simulate a noise-corrupted synthetic total-field anomaly (Figure 2.14a) produced by the depth-to-basement relief (Figure 2.14b) with one horst in the central portion and two grabens at different depths. The basement is constantly magnetized with an inclination of $5.0°$, a declination of $160.0°$ and intensity of $2.0\ \mathrm{A/m}$. We calculated the total-field (Figure 2.14a) of the simulated basement considering a geomagnetic field with inclination of $-3.5°$ and a declination of $-20.0°$. Hence, there is a strong remanent component. Note that, in this synthetic test, the inclination and declination of the geomagnetic field vector are close to the real case study from Pará-Maranhão Basin shown in Chapter 2 (sections 2.8 and 2.9). To calculate the observed total-field anomaly, we used the implementation of UIEDA et al. (2013), which is a prism-based implementation.

Like in the application to real data over Pará-Maranhão Basin, To determine an optimum inclination and declination of the magnetized basement, we perform a systematic and nonautomatic search of the data-misfit function on the plane of the inclination versus declination to map the optimum pair (or pairs) of inclination and declination as the one (or the ones) that yields the lowest value of the data-misfit function. Specifically, we perform the inversion on a coarse grid of 31 × 31 observation points in the north-south and east-west directions. We produce a discrete mapping of the data-misfit function ($\delta(\mathbf{p})$, equation 2.7) on the plane $m_i \times m_d$ (Figure 2.15a and 2.15b) considering an interval of inclinations varying from -30 to 30° and an interval of declinations varying from -180° to $180^{\circ}$of the magnetization vector of the basement. Figure 2.15 shows the mapping of $\delta(\mathbf{p})$ in logarithmic scale with a step of 10° for both m_i and m_d in Cartesian coordinates (Figure 2.15a) in polar coordinate (Figure 2.15b).

Like in the application real data from the Pará-Maranhão Basin (see Figure 2.10), we also have in this synthetic test two well-defined minima of the data-misfit measure (pinpointed as with stars in Figure 2.15a and 2.15b) are achieved when the

magnetization vector has an inclination of $-3°$ and a declination around 170° (close to the true magnetization direction of the basement) and another one with inclination of $-3°$ and declination of $-5°$.

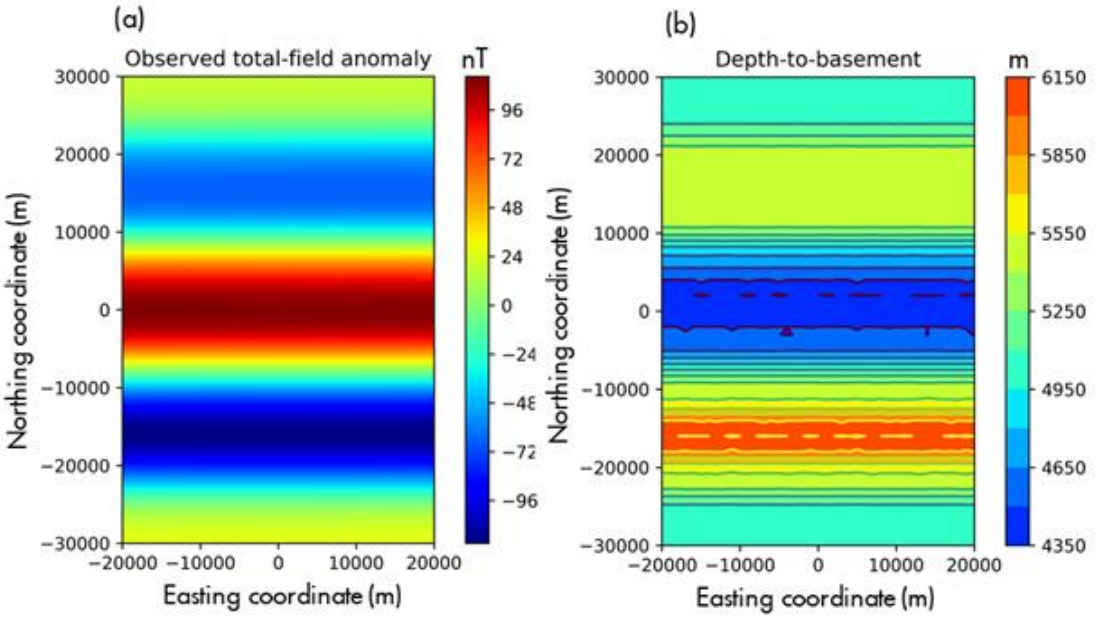

Figure 2.14: Observed total-field-anomaly (a) produced by the simulated basement relief (b).

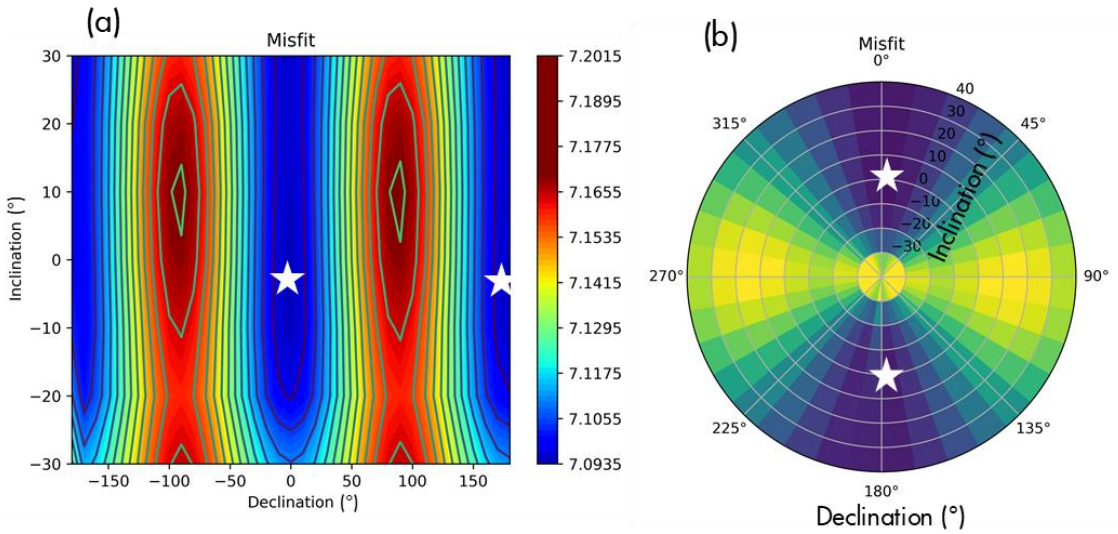

Figure 2.15: Contour maps of the logaritmic data-misfit function (log ($\delta(\mathbf{p})$), equation 2.7) on the plane $m_i \times m_d$ in Cartesian coordinates (a) and in polar coordinates (b). The white stars pinpoint the optimum pairs of the inclination and declination of the magnetized basement of the synthetic data (Figure 12.14a). The true magnetization direction has inclination of $5.0°$ and declination of $160.0°$.

Because we have two well-defined minima of the data-misfit measure (stars in Figure 2.15), two hypotheses of magnetization directions of the basement relief will be used to obtain two estimates of the magnetized basement relief.

In the first inversion, we assign to the magnetized basement the inclination of $-3°$ and declination of 170° (a star in Figure 2.15). Let us recall that this magnetization direction is close to the true one (inclination of 5.0°, a declination of 160.0°), which in turn differs from the geomagnetic field direction (with inclination of $-3.5°$ and a declination of $-20.0°$). Hence, we are testing the hypothesis of remanent magnetization with an assigned magnetization direction (inclination of $-3°$ and declination of 170°, a star in Figure 2.15) closes to the true one. Figure 2.16a shows that the predicted total-field anomaly yields an acceptable data fitting. In this test, the depth-to-basement estimate (Figure 2.16b) retrieves the true basement relief (Figure 2.14b) efficiently.

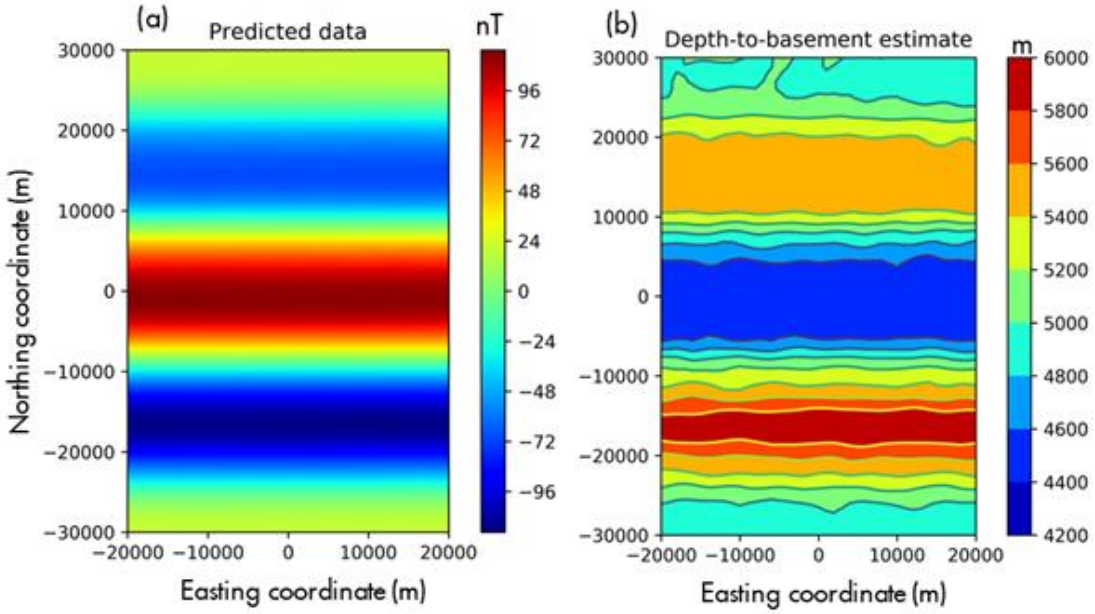

Figure 2.16: – Synthetic test - Under the hypothesis of remanent magnetization with inclination of $-3°$ and declination of 170° (star in Figure 2.15). Predicted total-field anomaly (a) produced by the estimated magnetic basement relief (b). The geomagnetic field direction has inclination of $-3.5°$ and declination of $-20.0°$. The true basement is magnetized with and inclination of 5.0° and declination of 160.0°.

In the second inversion, we assign to the magnetized basement the inclination of $-3°$ and declination of $-5°$ (a star in Figure 2.15). Let us recall that this assigned

magnetization direction differs either from the true one (inclination of $5.0°$, a declination of $160.0°$) or from the geomagnetic field direction (with inclination of $-3.5°$ and a declination of $-20.0°$). Hence, we are also testing the hypothesis of remanent magnetization; however, the assigned magnetization direction (inclination of $-3°$ and declination of $-5°$, a star in Figure 2.15) is wrong. Although, the assigned magnetization direction is wrong the predicted total-field anomaly yields an acceptable data fitting (Figure 2.17a). However, the depth-to-basement estimate (Figure 2.17b) does not retrieve the true basement relief (Figure 2.14b). Rather, the depth-to-basement estimate shown in Figure 2.17b, with a wrong magnetization direction picked from the discrete mapping of the data-misfit function (Figure 2.17), has an opposite geometry than the simulated basement (Figure 2.14b) and the estimated basement relief (Figure 2.16b) with a magnetization direction (picked from the discrete mapping of the data-misfit function) close the true one.

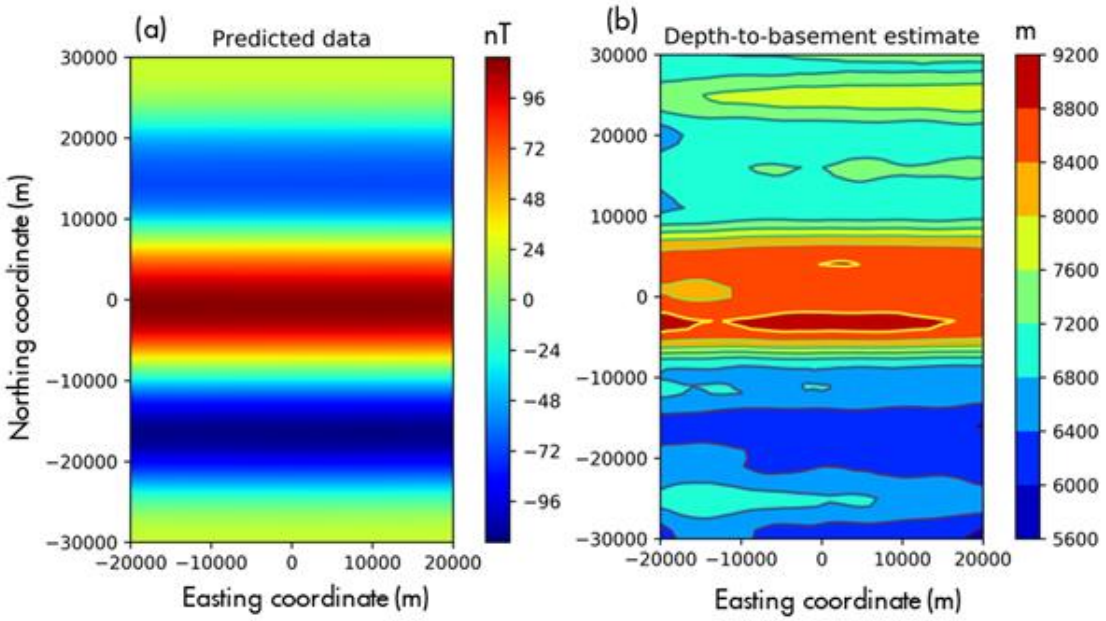

Figure 2.17: – Synthetic test - Under the hypothesis of remanent magnetization with inclination of $-3°$ and declination of $-5°$ (star in Figure 2.15). Predicted total-field anomaly (a) produced by the estimated magnetic basement relief (b). The geomagnetic field direction has inclination of $-3.5°$ and declination of $-20.0°$. The true basement is magnetized with and inclination of $5.0°$ and declination of $160.0°$.

We stress that the synthetic results shown in Figures 2.16 and 2.17 are similar to those obtained in the real data application (sections 2.8 and 2.9) where we have

two well-defined minima in the discrete mapping of the data-misfit function on the plane inclination versus declination (two stars in Figure 2.10). Both magnetization directions (two stars in Figure 2.10) yield acceptable data fittings (Figures 2.8b and 2.9b); however, the two depth-to-basement estimates (Figure 2.11) have an opposite geometry. One might think that the choice of the "best" depth-to-basement estimates might be difficult. However, we show that in the application to real data from Pará-Maranhão Basin the choice of the "best" depth-to-basement estimate was simple because we expect a seaward crustal thinning. Hence, only one depth-to-basement estimate (Figure 2.11a) exhibits this feature and consequently a seaward deeper basement.

Chapter 3

Magnetic amplitude inversion for depth-to-basement and magnetization intensity estimates

This chapter was submited for the Geophysics on November 2019.

3.1 Summary

We present an inversion method to recover both the depth and the total magnetization intensity of the basement under a sedimentary basin using the amplitude of the magnetic anomaly vector (amplitude data). Because the amplitude data is weekly dependent on the magnetization direction, the proposed method is suitable for interpreting areas with remanent magnetization. Our method assumes constant magnetized basement rocks overlain by nonmagnetic sediments. To overcome the inherent ambiguity of potential-field data, we assume the knowledge of the average depth of the basement and use it as a constraint to regularize the inversion. A sensitivity analysis with synthetic data shows the weak dependency of the magnetic amplitude inversion on the magnetization direction. Different combinations of magnetization

directions recover the interface separating sediments from basement rocks. Test on field data over the Foz do Amazonas Basin, Brazil, recovers the shape of the basement relief without any knowledge about the magnetization intensity and direction. The estimated basement relief reveals a smoothing basement framework with a local basement discontinuity, interpreted as a northwest–trending fault, and with clear gradient changes, interpreted as the transition between continental and oceanic crusts.

3.2 Forward model

We assume a sedimentary basin with no magnetic sediments or intrusions. We assume that its crystalline basement has a constant but unknown magnetization vector with inclination m_i, declination m_d and intensity m. Consider a Cartesian coordinate system with the $x-$ and $y-$ axes oriented, respectively, to the north and east, and the vertical axis ($z-$ axis) positive downward. We parametrize the magnetic basement with a collection of M prisms with tops at the interface between sediments and basement, and bottoms at an arbitrary constant depth Z_b tending to infinite. The depths of the tops of the prisms p_j, $j = 1, \dots, M$, define the basement relief and together with the magnetization intensity (m) are the parameters to be estimated from the amplitude of the magnetic anomaly vector.

To calculate the forward modeling of the α-component, $\alpha = x, y, z$, of the magnetic anomaly vector produced by a prism, we adopted the same methodology presented in Chapter 2 and published by Hidalgo-Gato and Barbosa (2019) to compute the total-field anomaly of a prism, which is named the fast-prismatic forward modeling. Like HIDALGO-GATO and BARBOSA (2019), we approximate the 3D integral (volume integral) of the α-component of the magnetic anomaly vector produced by the jth prism, at the observation point (x_i, y_i, z_i) with unity magnetization intensity and horizontal cross-section Δs, by a 1D integral along the prism thickness considering the limits of the integration as the depths to the top p_j (depth to the basement) at the jth prism and the depth to the base Z_b

$$b_{ij}^{\alpha} \approx C_m \, \Delta s \, \frac{\partial}{\partial \alpha} \int_{p_j}^{Z_b} \hat{\mathbf{h}} \cdot \nabla \frac{1}{r_{ij}} \, dz', \tag{3.1}$$

where $C_m = 10^9\mu_o/4\pi$ with μ_o as the vacuum permeability, $\hat{\mathbf{h}}$ is a unit vector defining the magnetization direction of all prisms with inclination m_i and declination m_d. In equation 1, $\boldsymbol{\nabla}$ is a three-dimensional gradient operator vector given by $\boldsymbol{\nabla} \equiv \left[\frac{\partial}{\partial x}, \frac{\partial}{\partial y}, \frac{\partial}{\partial z}\right]^T$ and

$$\frac{1}{r_{ij}} = \frac{1}{\sqrt{(x_i - x'_j)^2 + (y_i - y'_j)^2 + (z_i - z'_j)^2}}, \tag{3.2}$$

where x_i, y_i and z_i are the coordinates of the ith observation point, x'_j and y'_j are the horizontal coordinates of the center of the jth prism and z' is the integration variable representing the $z-$coordinate of an arbitrary point within the jth prism.

The amplitude of the magnetic anomaly vector due to the M prisms at the ith observation point (x_i, y_i, z_i), $i = 1, \ldots, N$, is given by:

$$d_i(\mathbf{p}, m) = m f_i(\mathbf{p}), \tag{3.3a}$$

where m is the uniform magnetization intensity of the prisms and

$$f_i(\mathbf{p}) = \sqrt{\left(\sum_{j=1}^{M} b_{ij}^x\right)^2 + \left(\sum_{j=1}^{M} b_{ij}^y\right)^2 + \left(\sum_{j=1}^{M} b_{ij}^z\right)^2}, \tag{3.3b}$$

in which $b_{ij}^{\propto}, \propto = x, y, z$, is defined by equation 3.1 and $\mathbf{p} = [p_1, \ldots, p_M]^T$ is a vector containing the depths to the top of the M prisms.

3.3 Inverse Problem

We consider the observed amplitude of the magnetic anomaly vector $\mathbf{d^o} = [d_1^O, \ldots, d_N^O]^T$ produced by a basement relief with constant magnetization vector having intensity m, inclination m_i and declination m_d. Let $\mathbf{d}(\mathbf{p}, m)$ be the N–dimensional vector of the predicted amplitude of the magnetic anomaly vector,

$$\mathbf{d}(\mathbf{p}, m) = m\,\mathbf{f}(\mathbf{p}), \tag{3.4}$$

whose ith element $d_i(\mathbf{p}, m)$ is given by equation 3.3a and $\mathbf{f}(\mathbf{p})$ is an $N \times 1$ vector whose ith element is defined by equation 3.3b.

Here, we wish to estimate the depths of the tops of the M prisms ($\mathbf{p}$) and the intensity of the magnetization vector (m) that better explain the observed amplitude data $\mathbf{d^0}$. Estimating the depths to the tops of M prisms from the observed amplitude data $\mathbf{d^0}$ to retrieve the shape of the basement relief is a nonlinear inverse problem. Conversely, estimating the magnetization intensity is a linear inverse problem. The ill-posedness of this problem is because of the inherent ambiguity involving attempts to estimate both the physical property and the volume of the source from any potential-field data. To reduce this ambiguity, we impose proximity between the estimated depths and a previously defined average depth Z_{avg}.

This problem is solved by minimizing the objective function

$$\varphi(\mathbf{p}, m) = \left\|\mathbf{d^0} - \mathbf{d}(\mathbf{p}, m)\right\|^2 + \mu\|\mathbf{p} - \mathbf{p^a}\|^2, \tag{3.5}$$

where $\|\cdot\|$ is the Euclidean norm, $\mathbf{p^a}$ is a M-dimensional vector with all elements equal to Z_{avg} and μ is a nonnegative scalar (regularizing parameter). The second Euclidean norm on the right side of equation 3.5 imposes a proximity between the estimated depths and the average depth Z_{avg}.

Expanding $\varphi(\mathbf{p}, m)$ in a Taylor series around the approximations $\mathbf{p}^k$ and m^k, at the kth iteration, and keep terms up to second order we get

$$\varphi(\mathbf{p}^k + \Delta\mathbf{p}^k, m^k + \Delta m^k) = \varphi(\mathbf{p}^k, m^k) + \mathbf{J_p^k}^T\Delta\mathbf{p}^k + J_m^k\Delta m^k +$$

$$\frac{1}{2}\Delta\mathbf{p}^{kT}\mathbf{H_{pp}^k}\ \Delta\mathbf{p}^k + \frac{1}{2}\Delta m^k H_{mm}^k\Delta m^k + \frac{1}{2}\Delta\mathbf{p}^{kT}\mathbf{h_{pm}^k}\ \Delta m^k + \frac{1}{2}\Delta m^k\mathbf{h_{mp}^k}^T\Delta\mathbf{p}^k, \tag{3.6}$$

where J_m^k is a scalar which contains the derivative of the function $\varphi(\mathbf{p}, m)$ with respect to m,

$$J_m^k = -2\,\mathbf{d^{0T}}\mathbf{f}(\mathbf{p}^k) + 2m^k\mathbf{f}(\mathbf{p}^k)^T\mathbf{f}(\mathbf{p}^k), \tag{3.7}$$

and $\mathbf{J_p^k}$ is the $M \times 1$ gradient vector of the function $\varphi(\mathbf{p}, m)$ with respect to vector $\mathbf{p}$,

$$\mathbf{J_p^k} = -2[\mathbf{A}^k]^{\mathrm{T}}[\mathbf{d^0} - m^k\mathbf{f}(\mathbf{p}^k)] + 2\mu(\mathbf{p^k} - \mathbf{p^a}), \tag{3.8}$$

where $\mathbf{A}^k$ is the $N \times M$ Jacobian matrix of the function $\mathbf{d}(\mathbf{p})$ with respect to vector $\mathbf{p}$. The ijth element a_{ij}^k of matrix $\mathbf{A}^k$ is the derivative of $\mathbf{d}(\mathbf{p})$ (equation 3.3b) with respect to the depth to the top of the jth prism p_j, i.e.,

$$a_{ij}^{k} = \frac{m^{k}}{\mathrm{f_i}(\mathbf{p}^{\mathrm{k}})}\left(\sum_{j=1}^{M} b_{ij}^{x}, \sum_{j=1}^{M} b_{ij}^{y}, \sum_{j=1}^{M} b_{ij}^{z}\right) \cdot \left(\frac{\partial}{dp_j} b_{ij}^{x}, \frac{\partial}{dp_j} b_{ij}^{y}, \frac{\partial}{dp_j} b_{ij}^{z}\right), \qquad (3.9a)$$

where · represents the dot product and the derivative part of equation 3.9a is

$$\left(\frac{\partial}{dp_j} b_{ij}^{x}, \frac{\partial}{dp_j} b_{ij}^{y}, \frac{\partial}{dp_j} b_{ij}^{z}\right) = \left(-\phi_i^{x}(p_j), -\phi_i^{y}(p_j), -\phi_i^{z}(p_j)\right), \qquad (3.9b)$$

where $\phi_i^{\alpha}(p_j)$, $\alpha = x, y, z$, is the α-component of the magnetic induction produced by a single jth dipole at the ith observation point. The jth dipole is magnetized by induction, with unitary magnetic moment and located at the top of the center of the jth prism whose depth is p_j. Like HIDALGO-GATO and BARBOSA (2019), the elements of the Jacobian matrix $\mathbf{A}^k$ have a simple analytic expression (equations 3.9a and 3.9b) that is more computationally efficient than the numerical approximation. In equation 3.6, H_{mm}^{k} is a scalar which contains the second derivative of the function $\varphi(\mathbf{p}, m)$ with respect to m

$$H_{mm}^{k} = 2\mathbf{f}(\mathbf{p}^{k})^{T}\mathbf{f}(\mathbf{p}^{k}), \qquad (3.10)$$

$\mathbf{H}_{\boldsymbol{pp}}^{\boldsymbol{k}}$ is the $M \times M$ Hessian matrix of the function $\varphi(\mathbf{p}, m)$ with respect to vector $\mathbf{p}$

$$\mathbf{H}_{\boldsymbol{pp}}^{\boldsymbol{k}} \approx 2\,\mathbf{A}^{k^{T}}\mathbf{A}^{k} + 2\mu\mathbf{I}, \qquad (3.11)$$

where $\mathbf{I}$ is the identity matrix of order M, $\mathbf{h}_{\boldsymbol{pm}}^{\boldsymbol{k}}$ is an $M \times 1$ vector containing the second derivatives of the function $\varphi(\mathbf{p}, m)$ with respect to $\mathbf{p}$ and m

$$\mathbf{h}_{\boldsymbol{pm}}^{\boldsymbol{k}} = -2\,\mathbf{F}^{k^{T}}\mathbf{d}^{\mathbf{0}} + 4m^{k}\,\mathbf{F}^{k^{T}}\mathbf{f}(\mathbf{p}^{k}), \qquad (3.12)$$

and $\mathbf{h}_{\boldsymbol{mp}}^{\boldsymbol{k}} = \mathbf{h}_{\boldsymbol{pm}}^{\boldsymbol{k}}$. In equation 3.12, $\mathbf{F}^{k}$ is the $N \times M$ Jacobian matrix of the function $\mathbf{f}(\mathbf{p})$ with respect to vector $\mathbf{p}$. All functions defined by equations 3.7 – 3.12 are evaluated at $\mathbf{p} = \mathbf{p}^{k}$ and $m = m^{k}$.

By differentiating the expanded function $\varphi(\mathbf{p}^{k} + \Delta\mathbf{p}^{k}, m^{k} + \Delta m^{k})$ (equation 3.6) with respect to $\Delta\mathbf{p}^{k}$ and Δm^{k} and setting the result equal to the null vector, we obtain the block linear systems of equations given by

$$\begin{bmatrix} H_{mm}^{k} & \mathbf{h}_{mp}^{k\,T} \\ \mathbf{h}_{pm}^{k} & \mathbf{H}_{pp}^{k} \end{bmatrix} \begin{bmatrix} \Delta\widehat{m}^{k} \\ \Delta\widehat{\mathbf{p}}^{k} \end{bmatrix} = -\begin{bmatrix} J_{m}^{k} \\ \mathbf{J}_{p}^{k} \end{bmatrix}, \tag{3.13}$$

where the caret denotes estimate. Here, to estimate the magnetization intensity perturbation Δm^k and the depth-to-basement perturbation $\Delta\mathbf{p}^k$, we solve the full linear system defined by equation 3.13 and update the magnetization intensity and depth-to-basement estimates iteratively as follows:

$$\widehat{\mathrm{m}}^{k+1} = \widehat{\mathrm{m}}^{k} + \Delta\widehat{\mathrm{m}}^{k}\,, \tag{3.14a}$$

and

$$\widehat{\mathbf{p}}^{k+1} = \widehat{\mathbf{p}}^{k} + \Delta\widehat{\mathbf{p}}^{k}. \tag{3.14b}$$

The stopping criterion is based on the invariance of the objective function (equation 3.5). At the iteration $k = 0$, the initial guest $\mathbf{p}^0$ of the basement depths is an M −dimensional vector with all elements equals to the average depth Z_{avg}.

We call attention to an interesting alternative approach to obtain the magnetization intensity and depth-to-basement estimates. This alternative approach is based on the fact that the vector $\mathbf{h}_{pm}^{k}$ (equation 3.12) containing the second derivatives of $\varphi(\mathbf{p}, m)$ with respect to $\mathbf{p}$ and m has elements close to zero (order of 10^{-8}). Hence, the two off-diagonal blocks in the linear system of equations 3.13 can be neglected. This yields to a block diagonal linear system which, in turn, results in two-step alternative approach for estimating the perturbations $\Delta\widehat{\mathrm{m}}^{k}$ and $\Delta\widehat{\mathbf{p}}^{k}$. In the first step, we solve a linear inverse problem by taking the estimate of magnetization intensity perturbation as

$$\Delta\widehat{m}^{k} = \widehat{m}^{k+1} - \widehat{m}^{k}, \tag{3.15}$$

and estimate the magnetization intensity by

$$\widehat{m}^{k+1} = \frac{\mathbf{d^0}^{T}\mathbf{f}(\mathbf{p}^{k})}{\mathbf{f}(\mathbf{p}^{k})^{T}\mathbf{f}(\mathbf{p}^{k})}. \tag{3.16}$$

In the second step, we solve a nonlinear inversion by using the iterative Gauss-Newton method with MARQUARDT (1963) strategy (SILVA et al., 2001; SILVA DIAS et al., 2007) for estimating the depths to the basement. This is accomplished by

estimating, at the kth iteration, the vector of the depth-to-basement perturbation $\Delta\widehat{\mathbf{p}}^k$ through the solution of the linear equation system

$$(\mathbf{H}_{pp}^{k} + \lambda^k \mathbf{I})\Delta\widehat{\mathbf{p}}^k = -\mathbf{J}_p^k \,, \tag{3.17}$$

where $\mathbf{J}_p^k$ and $\mathbf{H}_{pp}^{k}$ are given by equations 3.8 and 3.11, respectively and λ^k is a nonnegative number, known as Marquardt's parameter, which is automatically adjusted during the iterative process to guarantee that the modified Hessian matrix be positive definite and to ensure the convergence.

We stress that both the computation time and the estimated perturbations ($\Delta\widehat{m}^k$ and $\Delta\widehat{\mathbf{p}}^k$) obtained by solving the full linear system (equation 3.13) or by following the above explained alternative approach (equation 3.15-3.17) are approximately equal, in the same order of magnitude and both recovers satisfactory the true basement relief. Hence, we used the approximate alternative approach described before.

3.4 Determining the inversion hyperparameters

In an inverse problem, hyperparameters are variables whose values are set before running the inversion code. Hyperparameters have an impact on the inversion result but they are not directly estimated in the inversion. In our work, the hyperparameters are the regularizing parameter μ (equation 3.5), the average depth Z_{avg} (vector $\mathbf{p}^{\boldsymbol{a}}$ in equation 3.5) and the bottom depth Z_b (equation 3.1).

The regularizing parameter μ controls the solution stability and how close the estimated basement relief will be to the average depth Z_{avg}. The larger the value of μ, the more stable and the closer to the average depth Z_{avg} will be the estimated basement relief. To determine μ, we use the L-curve criterion (HANSEN, 1992) which consists in plotting, on a log–log scale, the squared norm of the regularized solution ($\|\widehat{\mathbf{p}} - \mathbf{p}^{\boldsymbol{a}}\|^2$) against the squared norm of the regularized data residual ($\left\|\mathbf{d}^{\mathbf{0}} - \mathbf{d}(\widehat{\mathbf{p}}, \widehat{m}\,)\right\|^2$) for a range of regularizing parameters. Typically, this plot resembles an L-shaped curve. The optimum value of μ is the one closest to the "corner" of the L-curve.

To determine the average depth Z_{avg} and the bottom depth Z_b, we use spectral method original proposed by BHATTACHARYYA and LEU (1977) and modified by OKUBO et al. (1985). BHATTACHARYYA and LEU (1977) presented a method for spectral analysis of gravity and magnetic anomalies due to 3D vertical prism. This method determines the depth to the top of the source from the linear slope of azimuthally averaged Fourier spectrum. We use this depth to the top of the source as the average basement depth Z_{avg}. BHATTACHARYYA and LEU (1977) also determine the depth to the centroid (Z_c) from the slope of an azimuthally averaged frequency-scaled Fourier spectrum in the low wavenumber region. Finally, the depth to the bottom of the source Z_b is determined by the difference between $2\,Z_c$ and the depth to the top of the source (here called Z_{avg}), i.e., $Z_b = 2\,Z_c - Z_{avg}$.

3.5 Application to synthetic data

To demonstrate and analyze the accuracy of our method, we apply it on a synthetic data simulating a rifted basin with non-magnetic sediments overlaying the basement relief. Figure 3.1 (vertically exaggerated) shows the simulated basement relief parametrized with a collection of prisms equally distributed in the $x-$ and $y-$ directions. All the prisms have the base at the constant surface $Z_b = 8\,km$. The basement relief in Figure 3.1 extends from -30 to $30\,km$ in the $x-$ and $y-$ directions. To minimize edge effects in the inverse problem, we extrapolate the model by $20\,km$ outside the shown area in both directions. Figure 3.2 shows the noise-corrupted amplitude of the magnetic anomaly vector produced by the simulated rifted basin with a constant magnetization vector having inclination, declination and intensity equals to $+45°$, $+20°$ and 2 A/m, respectively. The basement is magnetized by induction only. We use the implementation of UIEDA et al. (2013) to calculate the b_x, b_y and b_z components of the magnetic vector produced by the prisms on a regular observation grid of $0.5\,k$m $\times$ $0.5\,k$m at a $0.15\,k$m height. The anomaly is corrupted with pseudorandom zero-mean Gaussian noise with a standard deviation of 10 nT.

To invert the amplitude of the magnetic anomaly vector (Figure 3.2), we assume an average depth Z_{avg} equal to 3.51 km. This value is equal to the true average depth of the simulated basement relief. We also assume that the basement magnetization vector (inclination and declination) is known and constant. We parameterize the

simulated basement by discretizing it into a 100 × 100 grid of 3D vertical prisms in the $x-$ and $y-$directions, respectively, with the same horizontal dimensions of 1 km. This discretization model includes the extended area beyond the limits of the data.

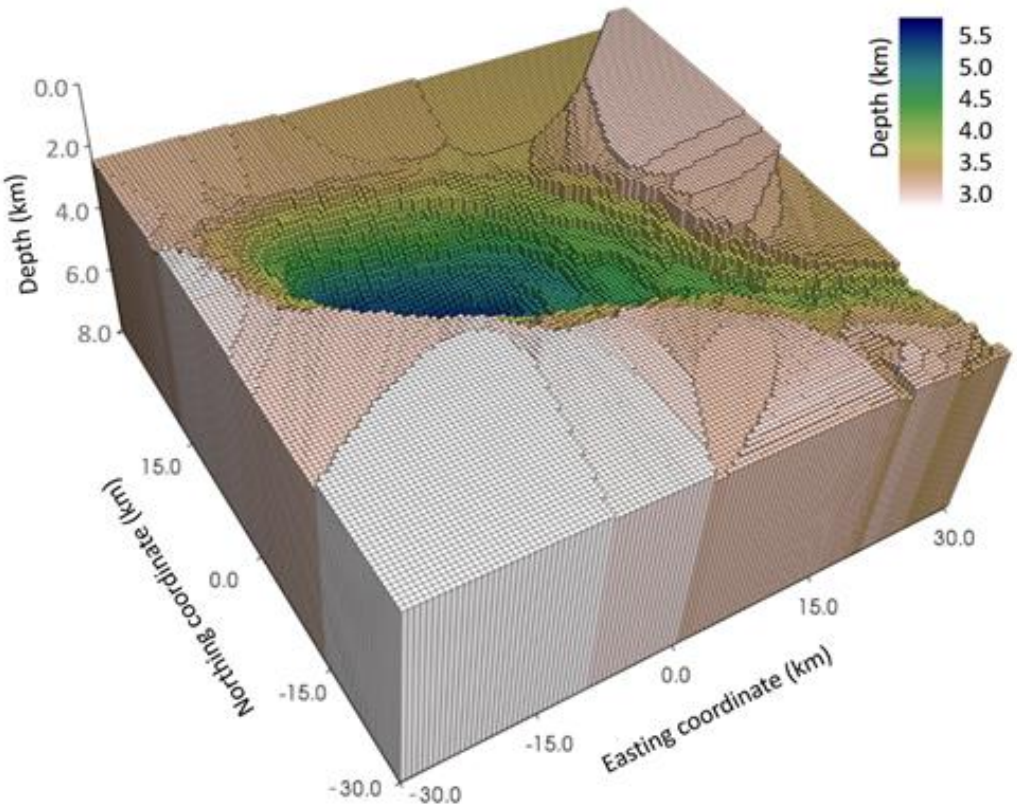

Figure 3. 1: Perspective view of the simulated basement relief.

Because we assume the true average depth of the sediment-basement interface, the magnetization intensity is not a sensitive parameter in our inverse problem and thus any initial constant guess of the magnetization intensity results in the same estimated basement relief for a given pair of inclination (m_i) and declination (m_d). We solved our inverse problem using $\mu = 0.01$, which was estimated through L-curve approach (HANSEN, 1992). The inversion converged within 11 iterations to misfit values close to the error level.

Figure 3.3 shows the estimated basement relief and the histograms of the differences between simulated (Figure 3.1) and estimated basement depths. The basement is recovered within less than ± 0.1 km differences (one standard deviation) and the histogram of depth residuals shows a sample mean close to zero and standard deviation of 0.078 km (Figure 3.3). As we can see, the predicted data (Figure 3.4) explain the observed (Figure 3.2) amplitude of the magnetic anomaly vector within the

error level regardless the wrong initial guess of the magnetization intensity (80 A/m). We recovered the magnetization intensity in the first iteration with high accuracy level (2.02 A/m).

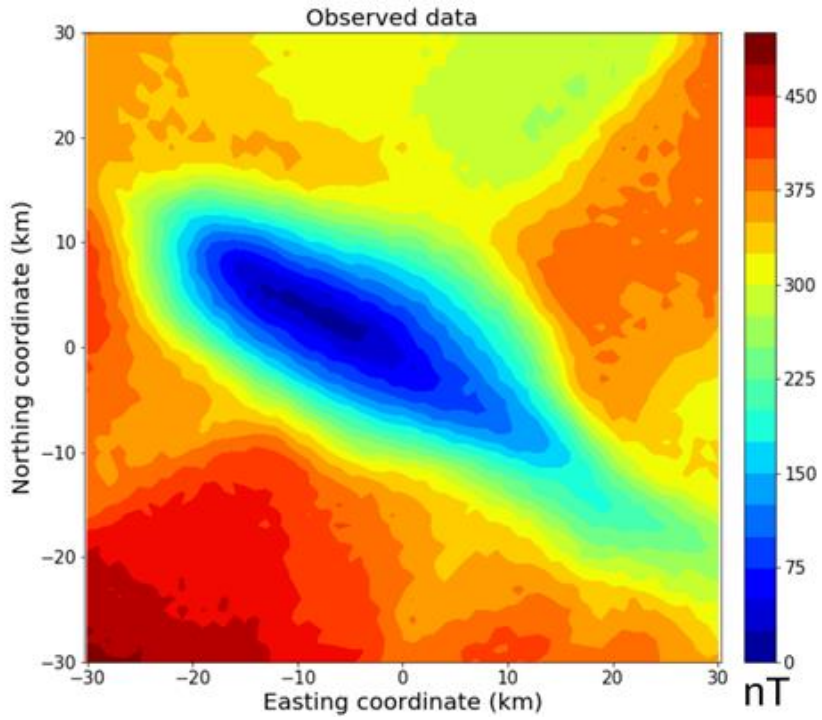

Figure 3.2: Observed noise-corrupted amplitude of the magnetic anomaly vector.

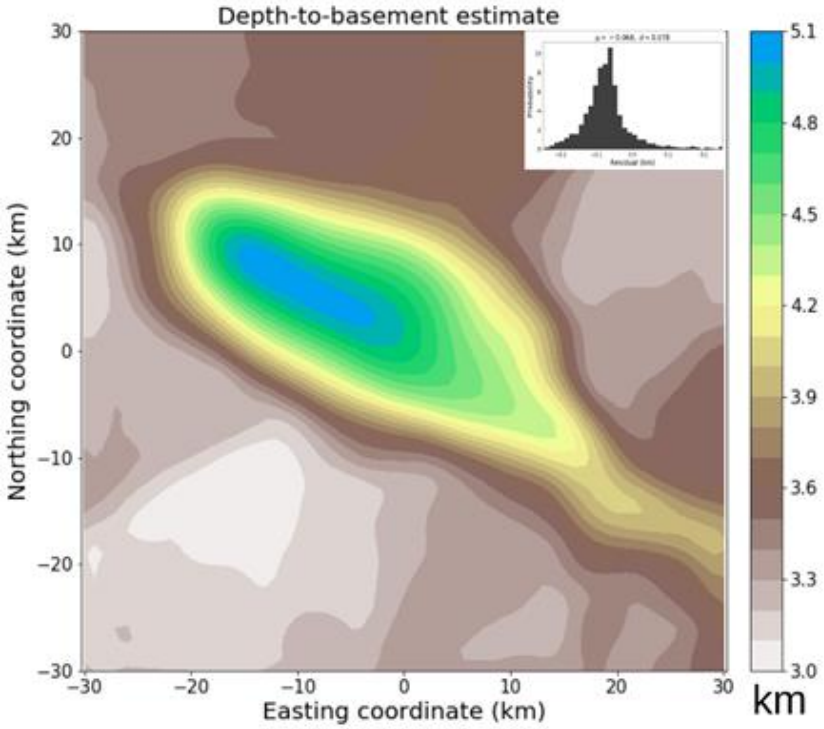

Figure 3.3: Depth-to-basement estimate. The inset shows the histogram of depth residuals

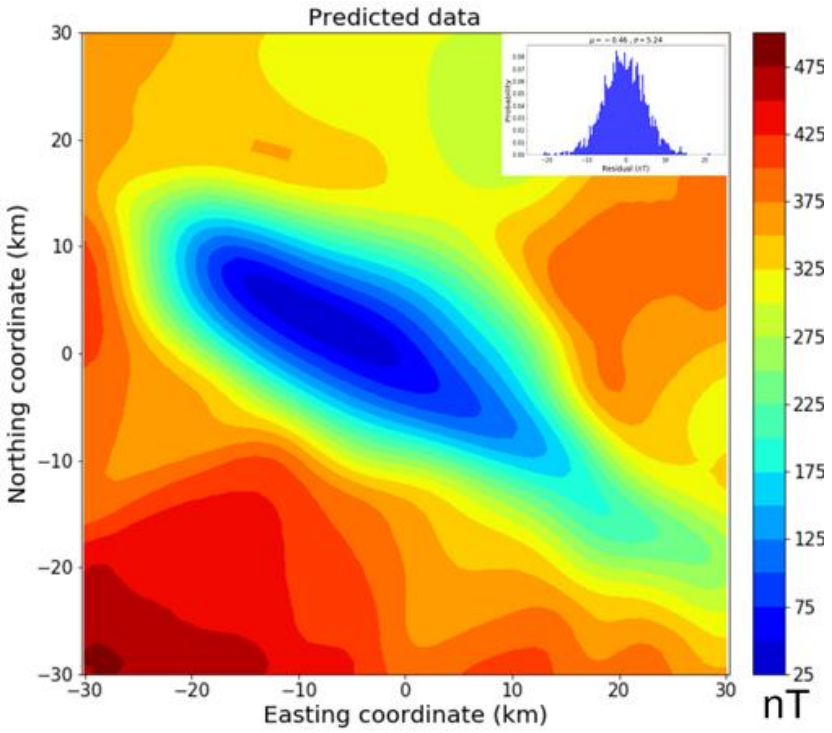

Figure 3. 4: Predicted amplitude of the magnetic anomaly vector. The inset shows the histogram of data residuals.

In Appendix 3.A We show a synthetic test with induced magnetization in low latitudes, like our real case data. We simulated a sequence of horst and grabens with different depths and inverted the amplitude data to recover the simulated basement relief.

Sensitivity analysis to the magnetization direction

To investigate the sensitivity of our method to the magnetization direction, we invert the observed amplitude of the magnetic anomaly vector (Figure 3.2) for different combinations of inclination m_i and declination m_d of the magnetization vector direction. Figure 3.5 and 3.6 display the results of this sensitivity analysis. Figure 3.5a shows the observed data (the same shown in Figure 3.2) produced by the true simulated basement relief shown in Figure 3.6a (the same shown in Figure 3.1) and the true basement-relief profiles (black line) whose locations are shown in the map (dashed lines in Figure 3.6a) of the true basement relief. Figures 3.5b and 3.6b show the inversion results by assuming known induced magnetization vector (i.e., $m_i = 45°$ and $m_d = 20°$, the same results shown in Figures 3.3 and 3.4). Figures 3.5c-3.5g and 3.6c-

3.6g show the solutions sensitivity to uncertainties in the magnetization inclination and declination. The wrong assigned magnetic inclinations m_i and declinations m_d of Figures 3.5c-3.5g and 3.6c-3.6g are shown in their corresponding title headings.

The three rows in Figure 3.5c to 3.5g show the predicted amplitudes of the magnetic anomaly vector (upper row), the histograms of the data residuals (middle row) and the data residuals (lower row); where the data residuals are the differences between observed (Figure 3.5a) and predicted (upper panels in Figure 3.5c-3.5g) data. The first and second rows in Figure 3.6c to 3.6g show, respectively, the estimated basement reliefs and model residuals defined as the differences between true basement relief (Figure 3.6a) and estimated basement reliefs (upper panels in Figure 3.6c-3.6g). For a more precise analysis, we plot the true (black line) and the estimated (blue line) basement reliefs in 2D profiles along the east-west and north-south directions as shown in the two lower rows of Figure 3.6c to 3.6g.

Figures 3.5c and 3.6c and Figures 3.5d and 3.6d show the inversion results by using a magnetization vector inclination equal to +45° (same as true one) and wrong declinations of -45° and +45°, respectively. Both, the wrong negative (Figure 3.6c) and the wrong positive (Figure 3.6d) declinations recover satisfactorily the basement reliefs within an acceptable error margin. This is corroborated by the histograms of the data residuals in Figure 3.5c and 3.5d, which show means and standard deviations close to zero. These results are by themselves a contribution over the existing inversion algorithms since we managed to recover the magnetic basement using a wrong declination of the magnetization vector.

The amplitude of the magnetic anomaly vector is weakly dependent on the magnetization vector direction but not fully independent, especially the opposite direction of the induced field as shown next. Figure 3.5e shows that even using a wrong magnetic inclination of +15° and a wrong magnetic declination of -20°, the depth-to-basement estimate (Figure 3.6e) recovers the simulated magnetic basement. One can notice that the estimated basement in Figure 3.6e is slightly different and less accurate than the estimates shown in Figure 3.6b-3.6d.

Let´s now consider a negative magnetic inclination. Figure 3.5f shows the inversion results using magnetic inclination and declination of -45° and +20°, respectively. Note that the magnetic inclination is in the opposite direction of the true one (+45°) and the magnetic declination is equal to the true one. As we can see in

Figure 3.5f the predicted amplitude of the magnetic anomaly vector explains the observed data within the data error level which is supported by the histogram of the data residuals and the map of data residuals. In contrast, the depth-to-basement estimate shown in Figure 3.6f is shifted towards the south-west direction when compared with true simulated basement relief. Similar behavior is observed in the estimated basement relief using an inclination of -30° and a declination of -45° as shown in Figures 3.5g and 3.6g. In this case, the basement relief is also shifted towards the south-west direction. However, both estimated basement reliefs shown in Figure 3.6f and 3.6g recover the shape of the true basement relief, but the estimates exhibit small shift.

The results shown in Figures 3.5 and 3.6 suggest that the depth-to-basement estimates by inverting the amplitude of the magnetic anomaly vector are more sensitive to uncertainties in the magnetic inclination than in the magnetic declination. Figures 3.5c and 3.6c and Figures 3.5d and 3.6d show that even considering uncertainties in magnetic declinations the amplitude data inversions retrieve the basement relief and fit the data. Conversely, Figures 3.5f and 3.6f and Figures 3.5g and 3.6g show that the amplitude data inversions with uncertainties in magnetic inclinations retrieve slightly dislocated shapes of the basement reliefs. The black arrows in Figure 3.6 show the gradients of the model residuals defined as the differences between true (Figure 3.6a) and estimated (upper panels in Figure 3.6b-3.6g) basement reliefs. The gradients are plotted in a regular grid over the maps of the model residuals (second row in Figure 3.6b-3.6g) where the gradients in the x- and y-directions define the direction of each arrow that points in the direction of steepest ascent and whose length is equal to the amplitude of the gradient scaled by a factor to improve the view of the arrows. Notice in Figure 3.6b that the arrows show the smallest lengths corroborating the excellent performance of the inversion of the amplitude data in estimating the basement relief by assuming the true magnetization vector (i.e., $m_i = 45°$ and $m_d = 20°$). Figure 3.6c and 3.6d shows arrow lengths smaller than ones shown in Figure 3.6f and 3.6g certifying that the amplitude data inversions are less sensitive to uncertainties in magnetic declinations (Figure 3.6c and 3.6d). The directions of the arrows in Figure 3.6f and 3.6g indicate the displacement of the estimated basement reliefs in the southwest-northeast direction. This gradient analysis (black arrows in Figure 3.6b-3.6g) is theoretical and cannot be applied to a field-data interpretation because it assumes the knowledge of the true basement relief.

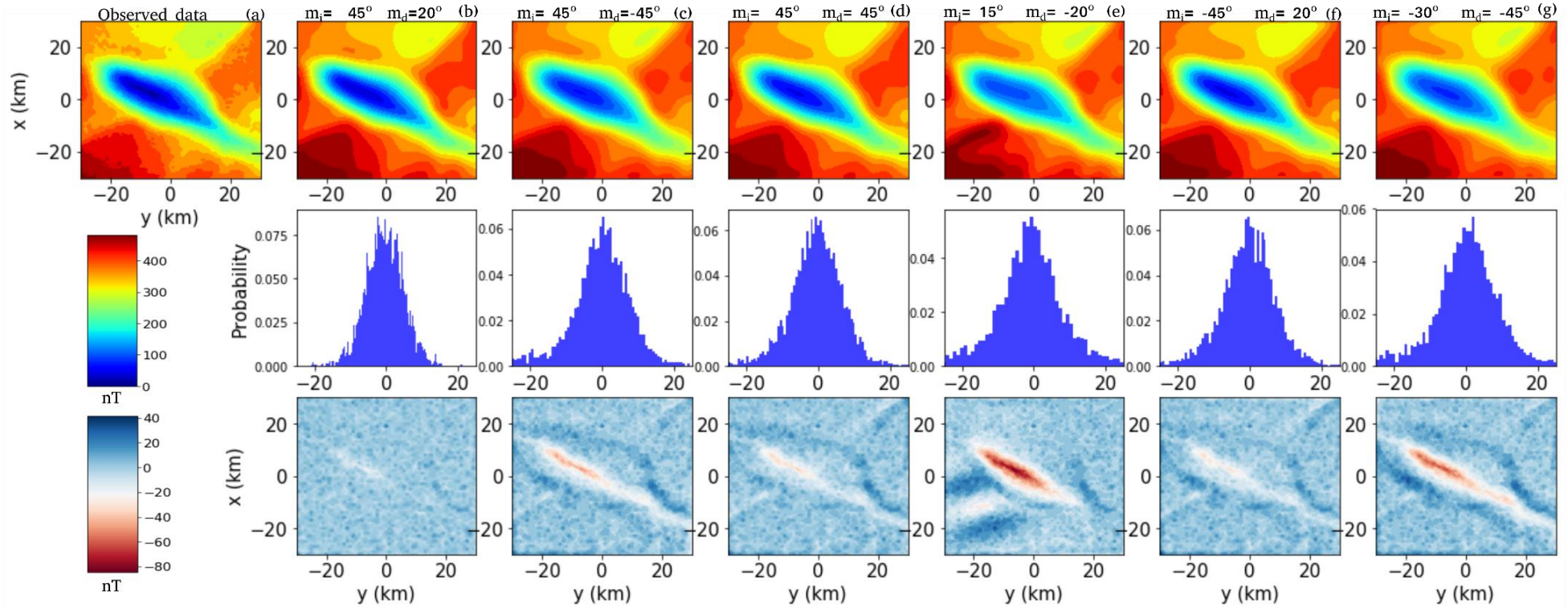

Figure 3.5: Magnetization direction sensibility on synthetic data. The first, second and third rows show, respectively, the observed (a) the predicted data (b to g) for different magnetization directions (magnetic inclinations m_i and declinations m_d are shown in the title headings of panels b to g) and (c) the histogram of the data residuals (observed minus predicted data) in nT. The true magnetization direction has inclination of $+45°$ and declination of $+20°$ (the estimate shown in panel b).

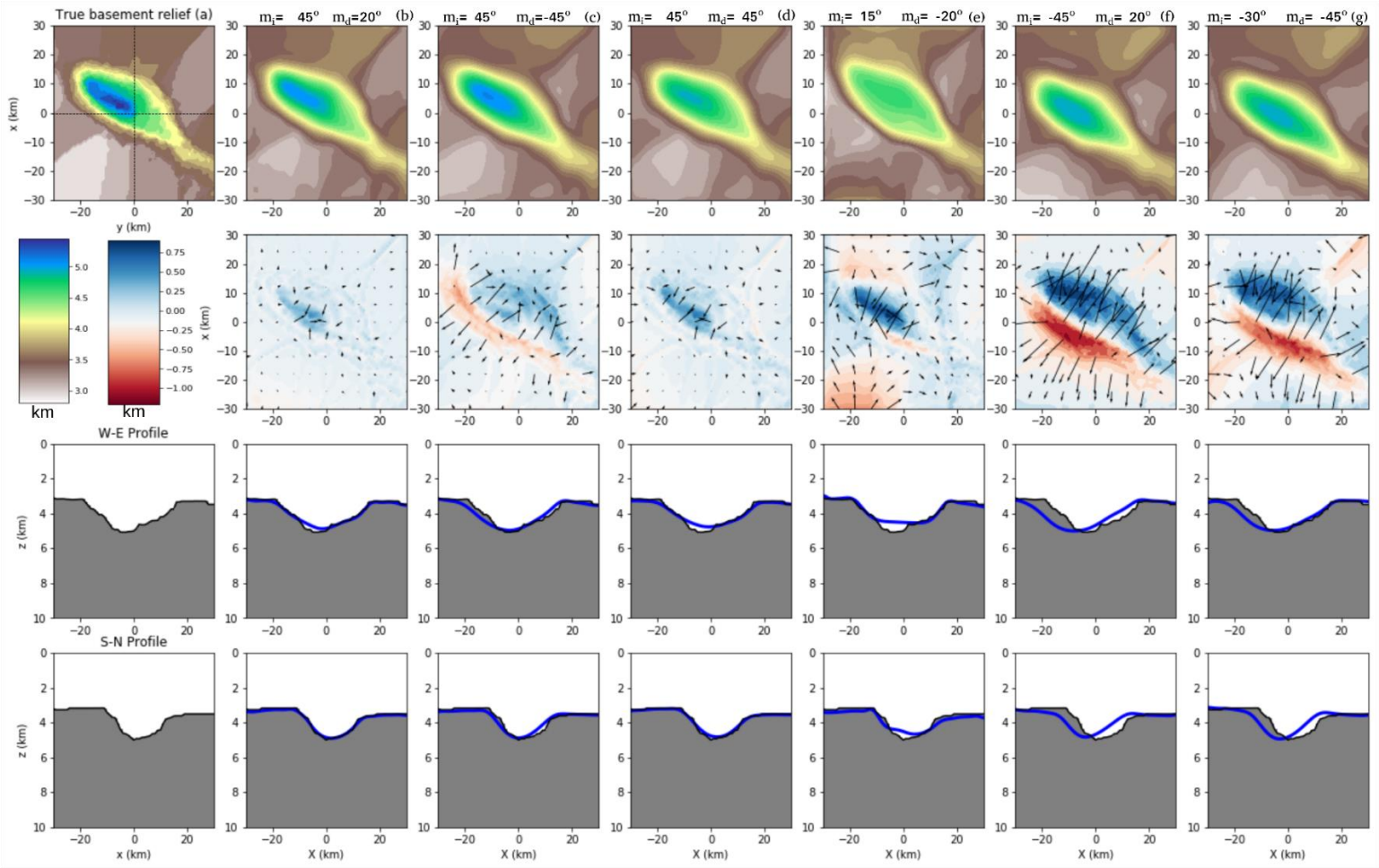

Figure 3.6: Magnetization direction sensibility on synthetic data. The first row shows the simulated (a) and estimated basement relief (b to g) for different magnetization directions (magnetic inclinations $m_i$and declinations $m_d$are shown in the title headings of panels b to g). The second row shows the model residuals (true minus estimated basement reliefs) in km. The black arrows show the gradients of model residuals. The two lower rows show east-west and south-north profiles extracted along the true (a) and estimated basement reliefs (b-g). The true and estimated basement reliefs in the profiles are shown in black and blue lines, respectively. The locations of these profiles are shown in dashed lines in the panel a.

Sensitivity analysis to the average depth

In the test shown in Figure 3.1-3.4, the average depth Z_{avg} of the simulated basement relief was assumed to be known. To investigate the sensitivity of our method to the average depth Z_{avg}, we invert the observed amplitude of the magnetic anomaly vector (Figure 3.2) by assuming a constant magnetization vector equal to the true one (inclination of +45° and declination of +20°) and a wrong average depth.

If the assigned average depth of the basement is shallower (Z_{avg} = 1.518 km) than the true one (3.51 km) the magnetization intensity estimate (0.5 A/m) is smaller than the true one (2 A/m) and the depth-to-basement estimate is shallower (Figure 3.7a) than the true one. Conversely, if the assigned average depth of the basement is deeper (Z_{avg}= 5.518 km) than the true one (3.51 km) the magnetization intensity estimate (5 A/m) is greater than the true one (2 A/m) and the depth-to-basement estimate (Figure 3.7b) is deeper than the true one. However, in both cases (shallower or deeper average depths than the true ones) the shapes of the estimated basement reliefs are very similar (Figure 3.7c) but the estimated depths present different averages.

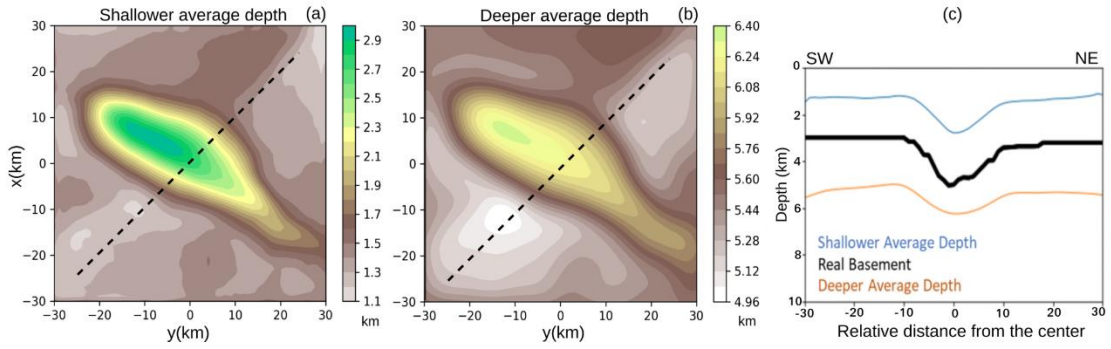

Figure 3.7: Average depth sensibility on synthetic data. Tests assigning incorrect average depths Z_{avg}. (a) $Z_{avg}$is shallower (1.518 km) than the true one and (b) Z_{avg} is deeper (5.518 km) than the true one. (c) The southwest-northeast profiles of the true basement relief (black line) and the estimated basements (color lines) shown in panels a and b. The location of these profiles is shown in dashed lines in the panels a and b. The true average depth of the basement relief is 3.51 km.

This sensitivity analysis to the average depth shows that our method estimates an apparent magnetization intensity of the basement rock.

3.6 Application to Field Data

Geological framework of the Foz do Amazonas basin

The Foz do Amazonas Basin is located between French Guiana to the north and the Pará-Maranhão Basin to the southeast. Figure 3.8 (modified from HIDALGO-GATO and BARBOSA, 2019) shows the five offshore basins that compound the Brazilian Equatorial Margin. The study area is located at the southeast portion of the Foz do Amazonas Basin (black square), a poorly studied portion of the basin extending from shallow to deep water. We access four public wells whose locations are shown in Figure 3.8 and their names are: 1APS10BAP (4255 m total depth), 1APS05AP (4354 m total depth), 1AS20BAP (3542 m total depth) and 1APS37AP (2255 m total depth). Unfortunately, none of the wells drilled deep enough to penetrate the basement rocks. Notwithstanding, none of four wells drilled in the study area have shown evidence of intrasedimentary igneous intrusions. The Foz do Amazonas Basin is a magma-poor basin as described by ZALAN (2017). Hence, the drill holes support the assumption of a nonmagnetic sediment layer overlaying the basement relief required by our method.

The tectonic framework of the entire Brazilian Equatorial Margin is linked to an oblique opening of the Atlantic Ocean, alternating between normal and strike-slips faults. The Precambrian basement of the Foz do Amazonas Basin consists of thrust belt faults in the north-northwest–south-southeast direction from the amalgamation of the Gondwana. COSTA et al. (2002) show a structural map with several normal faults and grabens in the onshore Foz do Amazonas and Marajó Basins. COSTA et al. (2002) suggest that the onshore portions of Foz do Amazonas and Marajó Basins have steep larger border faults and multi-tectonic phases during the basin evolution, which includes steps such as transtension, transpression and finalizing in another event of transtension during the Cenozoic. Indeed, there is a considerable tectonic complexity in the basement of the study area, which is part of the underexplored Brazilian Equatorial Basins.

Magnetic Data and basement relief estimation

The high-resolution magnetic data is a public airborne survey over the Foz do Amazonas Basin flown between 2003 and 2004. The acquisition lines in the study area are spaced by 2 km and flown in the N18°W direction at a constant average height of 150 m. Figure 3.8 shows the acquisition polygon (blue), the study area (black square) in Geographic coordinates and the total-field anomaly data in a local coordinate system that consist of a constant shift from the original UTM (51°W). The inclination and declination of the main geomagnetic field in the middle of the study area at the acquisition date were, respectively, 7.68° and -19.45. We gridded the data to the constant acquisition height of 150 m.

The spectral analysis (BHATTACHARYYA and LEU, 1977; and OKUBO et al., 1985) in the total-field anomaly data (Figure 3.8) shows that the average depth of the basement source (shallow-seated source) is at 6 km depth (Figure 3.9a) while the bottom of the magnetization (deep-seated source) is around 16 km depth (Figure 3.9b).

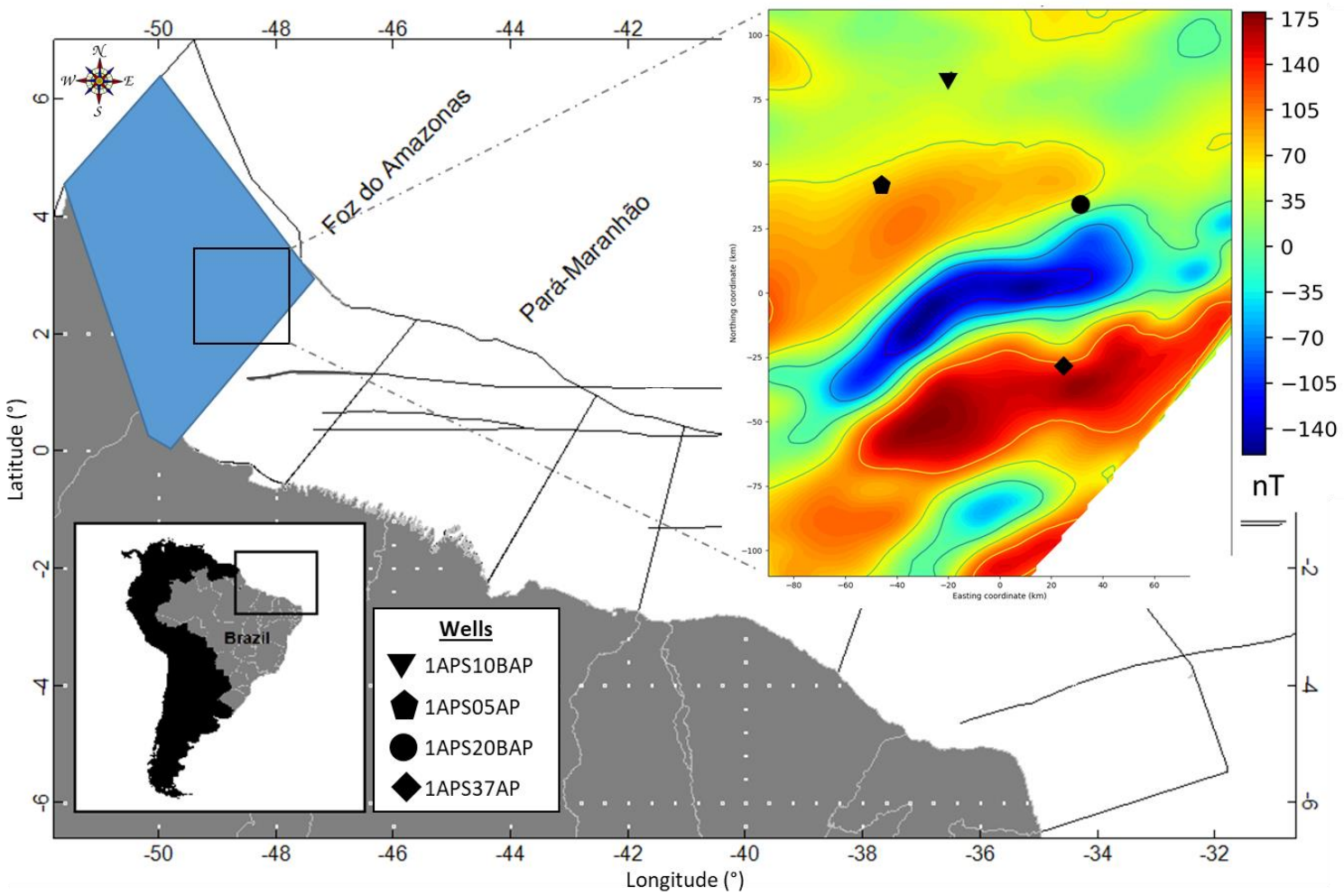

Figure 3.8: Location of the Foz do Amazonas Basin (Brazil) (Modified from HIDALGO-GATO and BARBOSA, 2019), the acquisition airborne survey (blue polygon), the study area (black square) and the total-field anomaly (colored map) of the study area with well locations (black symbols).

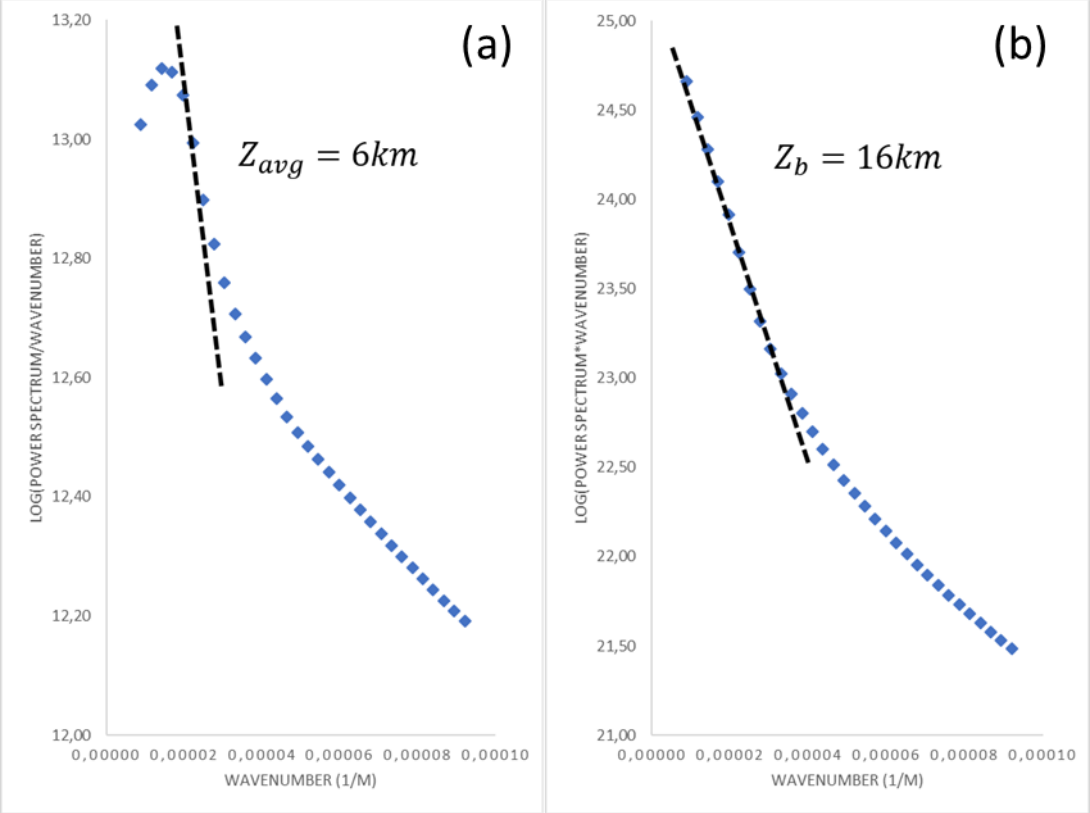

Figure 3. 9: The spectral analysis to determine (a) the average depth Z_{avg} and (b) the bottom depth Z_b.

By using the equivalent layer approach proposed by DAMPNEY (1969), we decompose the observed total-field anomaly (Figure 3.8) into the three orthogonal components of the magnetic vector bx, by and bz and then calculate the amplitude of the magnetic vector shown in Figure 3.10a.

The subsurface model is discretized as a collection of prisms with tops coincident with the average basement relief ($\hat{\mathbf{p}}^0$ = 6 km) and the bottom at the constant surface Z_b=16 km. The prisms are regularly spaced by 3600 m in both directions with a constant magnetization vector direction equal to the main geomagnetic field and intensity of 2 A/m (initial guess). We extrapolated the model by 50 km beyond the data limits in both horizontal directions to mitigate edge effects.

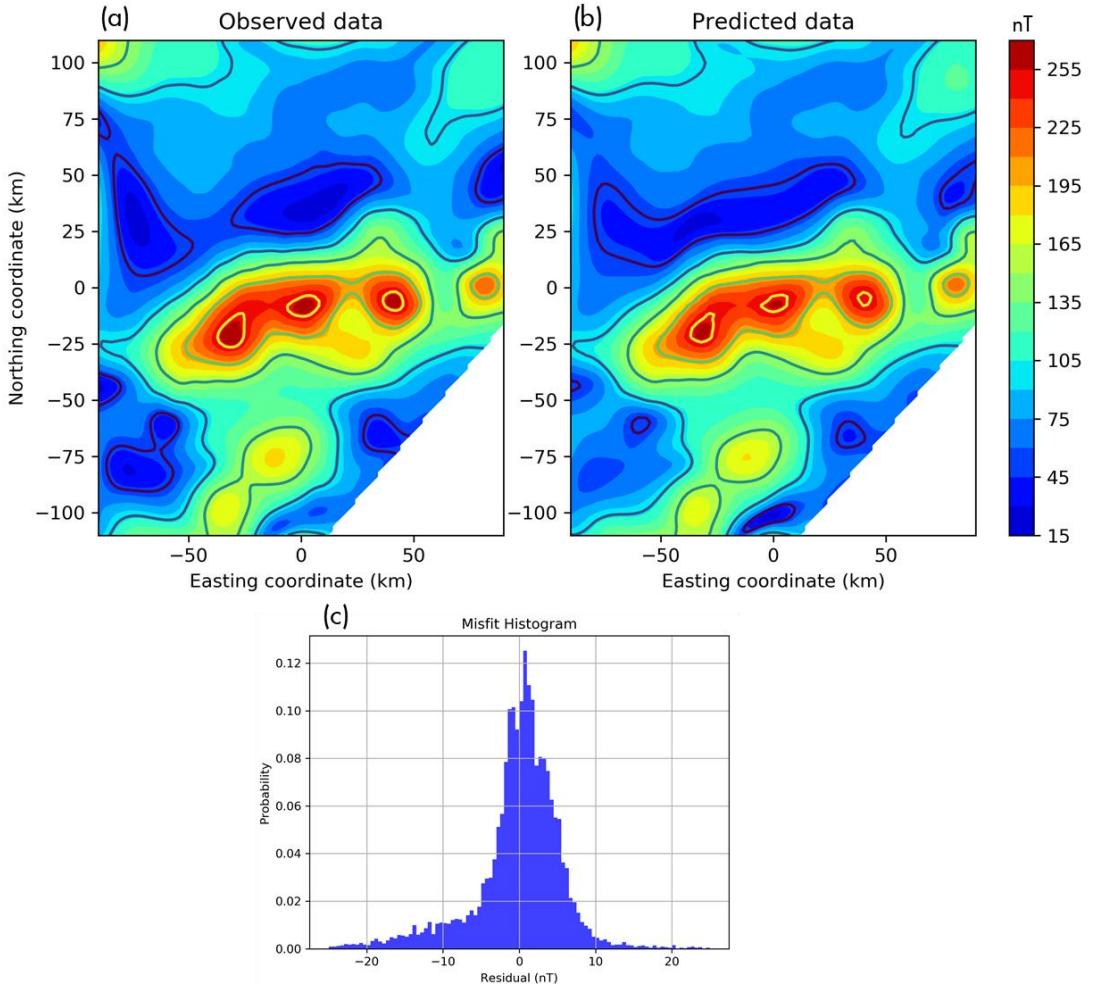

Figure 3.10: Observed (a) and predicted (b) amplitudes of the magnetic anomaly vector. (c) The histogram distribution of the data residual defined as the difference between observed (a) and predicted (b) data.

We inverted the amplitude of the magnetic vector (Figure 3.10a) to recover the basement relief using a regularization parameter μ=0.001 (estimated using L-curve proposed by HANSEN, 1992). The predicted amplitude of the magnetic vector (Figure 3.10b) explains the observed amplitude data (Figure 3.10a) within an acceptable error level. The histogram of the data residuals (Figure 3.10c), with zero mean and standard deviation of approximately 5 nT, corroborates the acceptance of the data fitting. The recovered apparent magnetization intensity is 4 A/m.

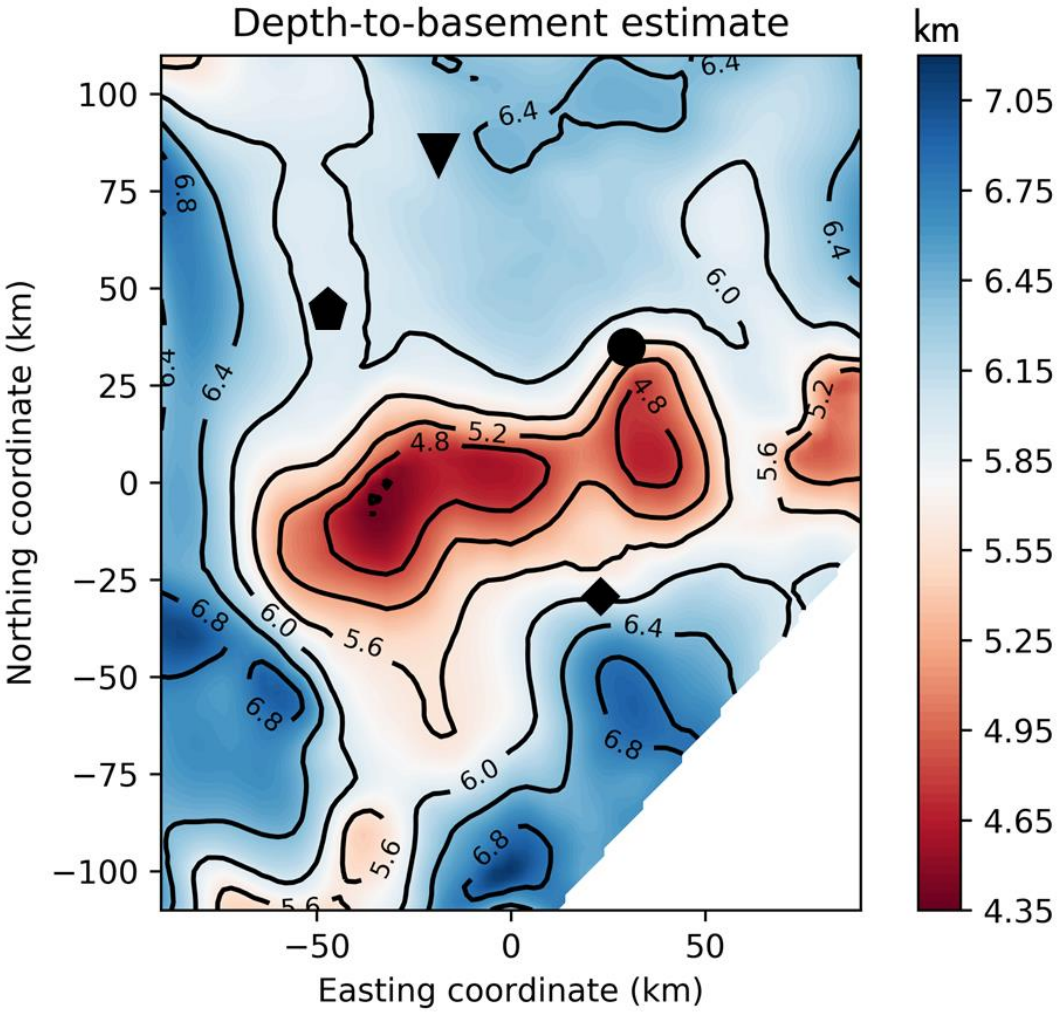

Figure 3.11: Contour map of the depth-to-basement estimate. The black symbols pinpoint the locations of the wells shown in Figure 3.8.

Figure 3.11 shows a map view of the depth-to-basement estimate with the proposed method with contour lines spaced by 400 m and the locations of the wells shown in Figure 3.8. Two basement highs are observed in the central part of the data. Note that the transition between basement highs and lows is smooth in most of the retrieved basement. In a regional-scale perspective, note that, at the northernmost limit, the estimated basement relief gets deeper and constant. We infer that this basement feature may be due to a change in crustal domains from a continental hyperextended crust to a more homogenous and monotonous oceanic crust.

3.7 Final considerations

In this Chapter, we proposed the inversion of the amplitude of the magnetic anomaly vector to estimate the depths and the apparent magnetization intensity of the magnetized basement of a sedimentary basin. We assume that the basement rocks have a constant magnetization vector throughout the study area. Our method is weakly dependent on the magnetization vector direction and intensity; hence, the precise knowledge about them is not required. The basement relief is approximated by a collection of vertical prisms with constant but unknown magnetization vector in both, direction and intensity. To overcome the ambiguity of inverting for volume and physical property inherent to potential field data our method requires the knowledge of the average depth of the basement relief.

We calculate the predicted amplitude of the magnetic anomaly vector through a fast approach that calculates a 1D integral over the prism thickness via the Gauss-Legendre Quadrature presented in Chapter 2. Our inverse problem uses the Gauss-Newton approximation with a proximity constraint to the average depth of the basement relief. We applied our inversion algorithm in a synthetic data simulating a rifted basin and performed a sensitivity analyses by changing the magnetization direction and the average depth of the magnetized basement. We show that the amplitude of the magnetic anomaly vector is weakly dependent, but it is not completely independent. Our inversion results suggest that the depth-to-basement estimates are more sensitive to uncertainties in the magnetic inclination than in the magnetic declination. Because of the fundamental ambiguity consisting of the product of the physical property (magnetization intensity) by the volume (basement layer), uncertainties in the average depth of the basement plays a significant role. If the assigned average depth of the basement is deeper (shallower) than the true one the magnetization intensity estimate is greater (smaller) and the depth-to-basement estimate is deeper (shallower) than the true ones. However, the shape of the estimated basement relief is very similar, regardless of the uncertainties in both the magnetization vector direction and the average depth of the basement.

We inverted a magnetic-amplitude dataset over the Foz do Amazonas Basin in the Brazilian Equatorial Margin. The amplitude dataset was calculated from the observed total-field anomaly in the space domain through equivalent layer approach. Our inversion estimates an overall smooth basement relief with a local basement discontinuity interpreted as an east-west trending fault. In regional scale, the gradient changes in the estimated basement relief seem to characterize the transition between continental and oceanic crusts.

The main limitation of the proposed method is the assumption about uniform magnetization of the basement rocks. The method estimates a single apparent magnetization intensity. Hence, a future improvement to the method includes to deal with intra-basement mafic and ultramafic bodies giving rise to strongly interfering magnetic anomalies.

3.8 Appendix 3.A: Synthetic Test at Low Latitude

In this thesis, we have applied the two developed inversions – the total-field anomaly inversion, in Chapter 2, and the magnetic amplitude inversion, in Chapter 3 – to synthetic data at middle latitudes and to field data at low latitudes. Here, we investigate the performance of our two inversions to synthetic data at low latitudes. Hence, we performed a synthetic test to invert 1) the total-field anomaly and 2) the amplitude of the magnetic vector for a common simulated basement relief. Figures 3.12c, 3.13c and 3.14c show the simulated depth-to-basement surface with one horst in the central portion and two grabens at different depths. The basement is constantly magnetized with and inclination of $5°$, a declination of $160.0°$ and intensity of $4.0\,\mathrm{A/m}$. We calculated the magnetic components of the simulated basement considering a geomagnetic field with inclination of $-3.5°$ and a declination of $-20.0°$; hence, there is a strong remanent component. Note that the inclination and declination of the geomagnetic field vector are close to the real case study shown in Chapter 2 (Para-Maranhao Basin) and Chapter 3 (Foz do Amazonas Basin). The base of the magnetic layer Z_b is a constant surface at 9 km depth. To calculate the observed data, we used the implementation of UIEDA et al. (2013), which is a prism-based implementation.

1) Depth-to-basement estimates from the total-field anomaly inversion (Chapter 2):

   Figure 3.12a shows the total-field anomaly produced by the basement relief (Figure 3.12c) calculated at a constant height of $-150\ m$. The observed data is corrupted with pseudorandom zero-mean Gaussian noise with a standard deviation of 1 nT. To minimize edge effects, we extrapolate the model to a constant grid that extends from -50 km to 50 km with a regular space of 2 km in both directions. Our starting guess is a constant surface at 5 km depth. In this first test, we assume the magnetization vector direction is known. We inverted the observed data using the GLQ method proposed in Chapter 2 with a number of nodes $n = 4$. Our iterative inversion runs over 3 iterations using a first-order Tikhonov regularization parameter of 0.00001. Figure 3.12b shows the predicted total-field anomaly produced by the depth-to-basement estimates (Figure 3.12d). The histogram of the residuals between observed and predicted data is shown in Figure 3.12b as an inset.

We can observe that the residuals follow a Gaussian distribution with mean around zero and standard deviation of less than 0.25 nT (one standard deviation). We can also note that the simulated basement relief (Figure 3.12d) was recovered successfully.

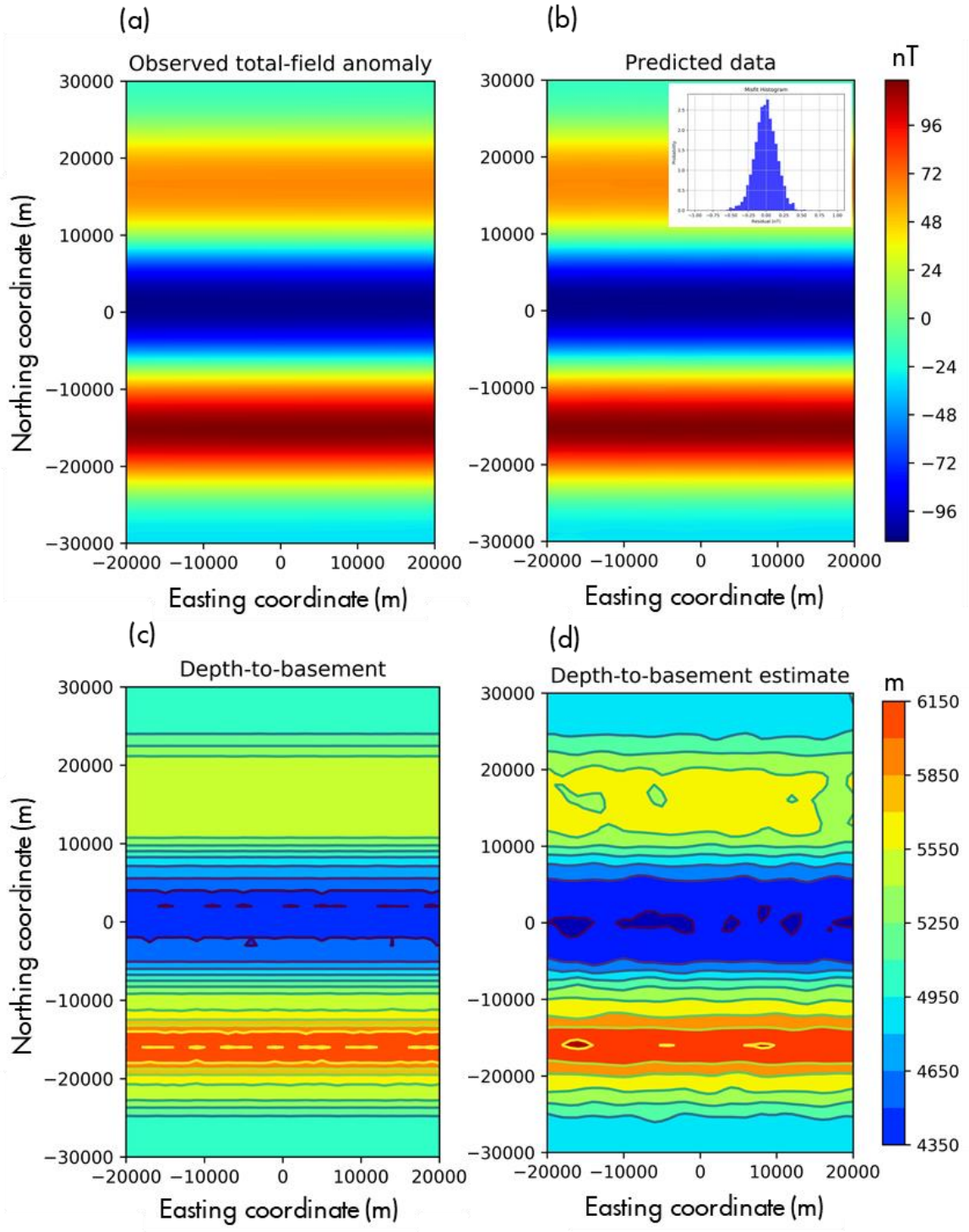

Figure 3.12: Inversion of the total-field anomaly at low latitudes with Gauss Legendre Quadrature method proposed in Chapter 2. The magnetization vector direction and intensity are known. (a) The observed and (b) predicted total-field anomalies. The observed anomaly,

in panel a, is produced by the simulated depth to basement (c). The predicted anomaly, in panel b, is produced by the estimated depth to the basement. The histogram distribution of the data residual (inset in b) is defined as the difference between observed (a) and predicted (b) total-field anomalies.

Figure 3.13 shows the inversion results in the case that the magnetization direction is unknown. Hence, we wrongly considered an induced magnetization (i.e., the magnetization vector of the basement is in the same direction of the geomagnetic field). Note that the observed (Figure 3.13a) and predicted (Figure 3.13b) total-field anomalies are very similar within the error level as shown by the histogram in Figure 3.13b. However, the estimated basement relief (Figure 3.13d) differs from the real basement (Figure 3.13c) either in its shape or in its depth. Note that the retrieved basement has an opposite polarity than the simulated basement. Under the wrong hypothesis of an induced magnetization, the simulated grabens and horst in Figure 3.13c are, respectively, retrieved as horsts and graben in Figure 3.13d

In most of the real case studies, the magnetization direction vector is unknown, and the magnetization is assumed to be purely induced. In Appendix 2.B, we performed a synthetic test showing the proposed magnetization estimation search method used in the real case study of Chapter 2.

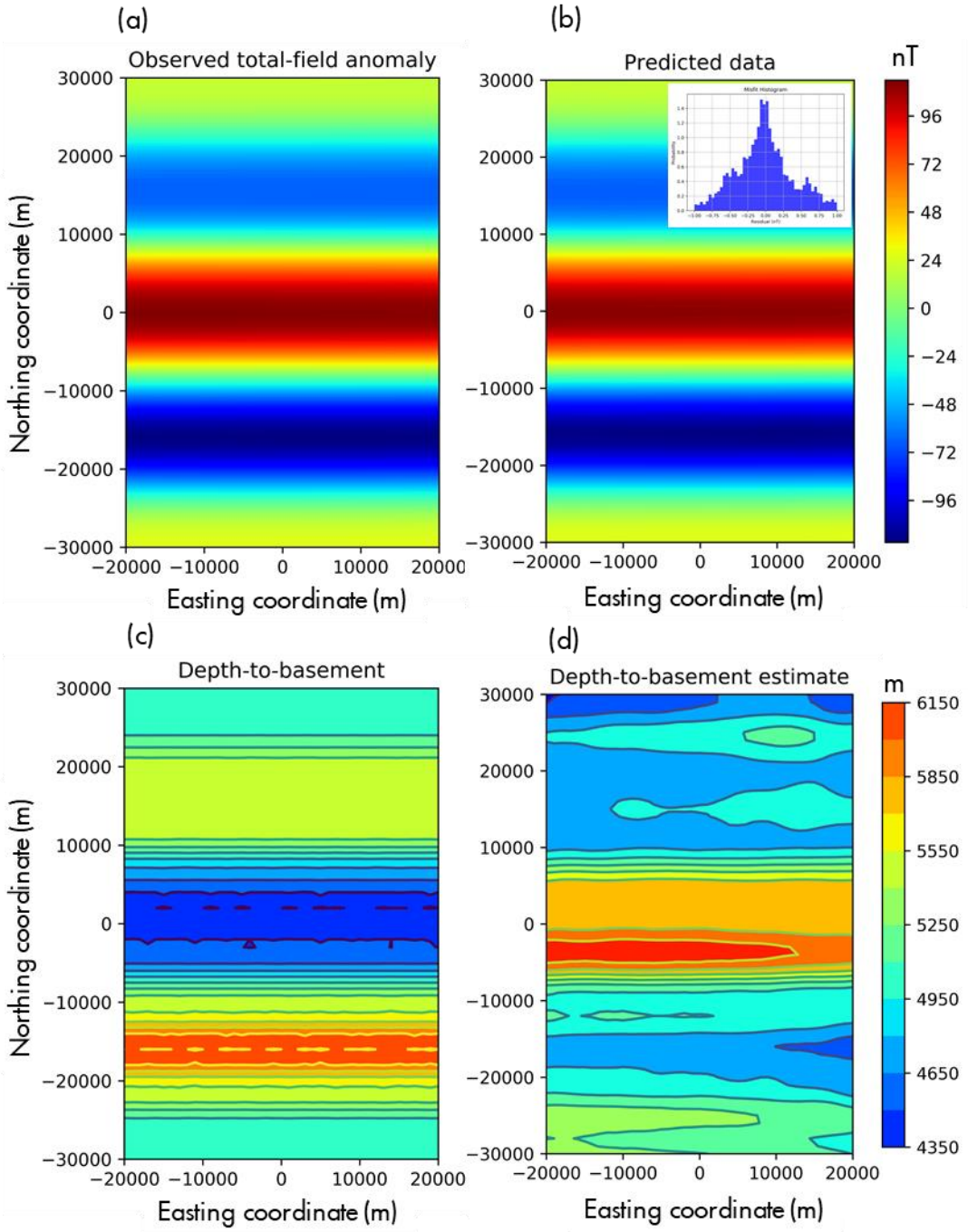

Figure 3.13: Inversion of the total-field anomaly at low latitudes with Gauss Legendre Quadrature method proposed in Chapter 2. The total-field anomaly inversion assumes a wrong hypothesis of induced magnetization. (a) The observed and (b) predicted total-field anomalies. The observed anomaly, in panel a, is produced by the simulated depth to basement (c). The predicted anomaly, in panel b, is produced by the estimated depth to the basement. The histogram distribution of the data residual (inset in b) is defined as the difference between observed (a) and predicted (b) total-field anomalies.

2) Depth-to-basement estimates from the amplitude data inversion (Chapter 3):

Figure 3.14a shows the amplitude of the magnetic anomaly vector (amplitude data) produced by the simulated basement relief shown in Figure 14c. We use the implementation of UIEDA et al. (2013) to calculate the bx, by and bz components of the magnetic vector produced by the collection of prisms. The amplitude data is corrupted with pseudorandom zero-mean Gaussian noise with a standard deviation of 1 nT. We extended the model from -50 km to 50 km in both directions on a regular spaced grid of 2 km. We parametrize the subsurface by a collection of regular prisms with constant tops at the average depth of the simulated basement relief with lateral size dx and dy equals to 2 km. Note that the lateral size of the prisms are at least two times less than the minimum depth of the simulated basement ($4350\ m$). To recover the basement relief, we invert the amplitude data using the GLQ approach presented in Chapter 3, with a starting magnetization intensity of $8.0\ A/m$, which is two times greater than the real magnetization intensity. Since the amplitude data inversion method is weakly dependent on the magnetization vector direction, we can assume an induced magnetization, i.e., we use the geomagnetic field direction as the magnetization vector direction. Our inversion requires a minimum of three iterations to converge using the true average depth and using a regularizing parameter of 0.00001. Figure 3.14b shows the predicted amplitude data calculated using GLQ method and produced by the estimated basement relief shown in Figure 3.14d. We can notice that the predicted data (Figure 3.14b) explains the observed amplitude data (Figure 3.14a) within the error levels as shown in the histogram distribution of the residuals in Figure 3.14b (inset). We can note high wavenumber features in the retrieved basement relief (Figure 3.14d). This is mainly because we did not impose a smoothness regularization and used a small regularizing parameter. Despite of that, the recovered basement relief follows the simulated basement with high accuracy. We emphasize that the simulated basement has a strong remanent component (inclination of 5° and declination of $160.0°$) which is different of the geomagnetic field (inclination of $-3.5°$ and a declination of $-20.0°$). Our inversion does not require the knowledge of the magnetization vector direction; hence, we used the induced field direction to invert the observed amplitude data. Despite of using a wrong magnetization direction, our method recovers the basement relief in shape

and in depth. These results could not be achieved by inverting a total-field anomaly data (Chapter 2) without using the correct magnetization direction as shown previously in Figures 3.12 and 3.13.

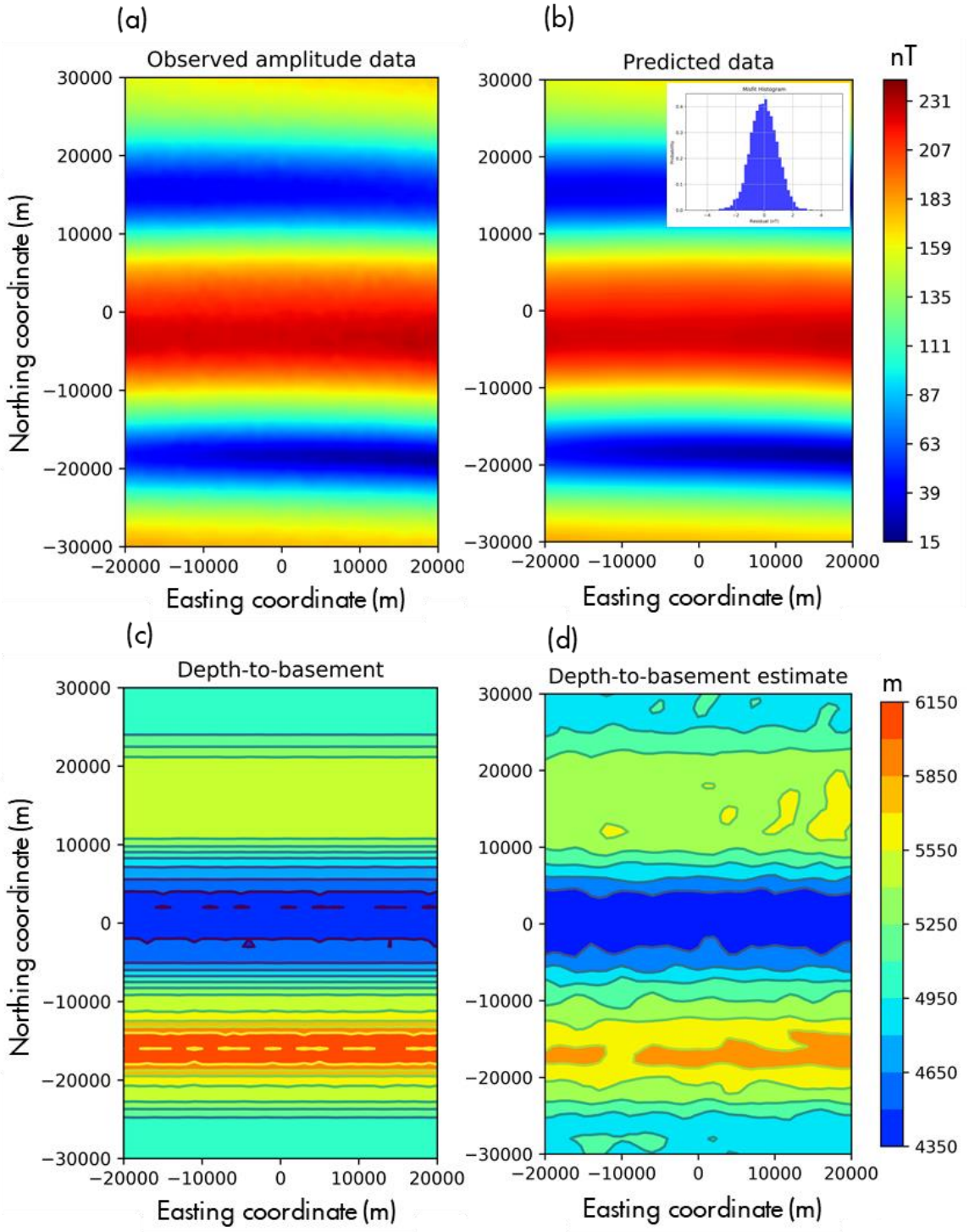

Figure 3.14: Inversion of the amplitude data at low latitudes with Gauss Legendre Quadrature method proposed in Chapter 3. The amplitude data inversion assumes a wrong hypothesis of induced magnetization. (a) The observed and (b) predicted amplitude data.

The observed amplitude data, in panel a, is produced by the simulated depth to basement (c). The predicted amplitude data, in panel b, is produced by the estimated depth to the basement. The histogram distribution of the data residual (inset in b) is defined as the difference between observed (a) and predicted (b) amplitude data.

Chapter 4

Conclusions

We developed two regularized nonlinear magnetic inversions to estimate the depths of the magnetic basement of a sedimentary basin with nonmagnetic sediments and without intra-sedimentary igneous intrusions. We approximated the basement layer by a grid of 3D vertical prisms juxtaposed in the horizontal directions of a right-handed coordinate system. The computational efficiency of our inversions is higher because we used an efficient way to compute the forward modeling of the magnetic data produced by a prism. The volume integral of the magnetic data of a prism was simplified by a 1D integration taken with respect to the z-axis of a prism (prism thickness) which is multiplied by the horizontal area of the prism.

The first method (Chapter 2) inverts the total-field anomaly by using the first-order Tikhonov regularization to estimate the depths of the magnetic basement. This inversion requires previously knowledge of the magnetization vector direction and intensity. For determining the inclination (m_i) and declination (m_d) of the magnetization vector of the basement layer, we constructed a discrete mapping of the data-misfit function on a plane $m_i \times m_d$ for intervals of $m_i \in [-50°, 50°]$ and $m_d \in [-180°, 180°]$. The best pair (m_i,m_d) is the one that yields the minimum of the mapped data-misfit function. We applied our inversion algorithm to a complex synthetic data and to a real data from the Pará-Maranhão Basin (Brazil). The estimated basement relief of the sedimentary basin looks geologically reasonable.

The second method (Chapter 3) inverts the amplitude of the magnetic anomaly vector to estimate simultaneously the depths and the magnetization intensity of the magnetized basement of a sedimentary basin. We assumed that the basement rocks have a constant magnetization vector. We showed that our method is weakly dependent on the magnetization vector direction and intensity; hence, no previous knowledge about them is required. To minimize the ambiguity of estimating the volume and the physical property, inherent to potential-field data, our method requires the knowledge of the average depth of the basement relief. Tests on synthetic and field data from the Foz do Amazonas Basin in the Brazilian Equatorial Margin showed the applicability of our method.

We showed that the total-field anomaly inversion (Chapter 2) is highly dependent on the knowledge of the magnetization vector direction. Our tests showed that the inversion of the total-field anomaly can estimate a completely wrong basement relief under wrong hypotheses of magnetization direction. The sensitivity analysis of the total-field anomaly inversion showed its robustness to the choice of the initial guess that can be a planar surface at any depth. However, the sensitivity analysis to uncertainties in the magnetization contrast of the magnetic basement showed that the total-field anomaly inversion is highly dependent on its knowledge. Although there is a high dependence, the consequences to uncertainties in the knowledge about the magnetization contrast are trivial. By assigning a magnetization contrast smaller than the true one, the estimated basement relief via the total-field anomaly inversion is shallower when compared with the true one. Conversely, by assigning a magnetization contrast larger than the true one, the estimated basement relief via the total-field anomaly inversion is deeper than the true one.

Conversely, we showed that the inversion of the amplitude of the magnetic anomaly vector (Chapter 3) is weakly dependent on the magnetization vector direction; hence, it does not require previous knowledge about the direction of magnetization vector (declination, inclination). Our tests showed that the inversion of the amplitude of the magnetic anomaly vector is weakly dependent; however, it does not mean a complete independence. The results suggested that the depth-to-basement estimates via the amplitude data inversion are more sensitive to uncertainties in the magnetic inclination than in the magnetic declination. The inversion of the amplitude of the magnetic anomaly vector estimates simultaneously the depths to the basement relief and the apparent magnetization-intensity of a sedimentary basin. To overcome the

inherent ambiguity of potential-field data involving the product of the physical property (magnetization intensity) by the volume (basement layer), we assumed the knowledge of the average depth of the basement and use it as a constraint to regularize the inversion. Although there is a high dependence on the knowledge of the average depth of the basement, the consequences to uncertainties its value are trivial. By assigning an average depth of the basement deeper (shallower) than the true one the magnetization intensity estimate is greater (smaller) and the depth-to-basement estimate is deeper (shallower) than the true ones. However, the shape of the estimated basement relief is quite similar, regardless of the uncertainties in both the magnetization vector direction and the average depth of the basement.

We stress that the main limitation of the two inversions is the assumption about uniform magnetization of the basement rocks either in the direction or in the intensity. Hence, a future improvement to these inversions could be taken into account the presence of intra-basement mafic and ultramafic bodies giving rise to strongly interfering magnetic anomalies.

Bibliography

ABRAMOWITZ, I. A.; STEGUN, M. A., 1972, "Handbook of mathematical functions", *Dover Publications*.

ALI, M. Y.; FAIRHEAD, J. D.; GREEN, C. M.; NOUFAL, A., 2017," Basement structure of the United Arab Emirates derived from an analysis of regional gravity and aeromagnetic database", *Tectonophysics*, 712–713, 503–522, doi: 10.1016/j.tecto.2017.06.006.

ASTER, R. C.; BORCHERS, B., AND THURBER C. H., 2005, "Parameter estimation and inverse problems", International Geophysics: Academic Press.

BANSAL, A. R.; GABRIEL, G.; DIMRI, V. P.; KRAWCZYK, C. M., 2011, "Estimation of the depth to the bottom of magnetic sources by a modified centroid method for fractal distribution of sources: An application to aeromagnetic data in Germany", GEOPHYSICS, 76, 11-22.

BARBOSA, V. C. F.; SILVA, J. B. C., 1994, "Generalized compact gravity inversion", *GEOPHYSICS*, 59, 57–68, doi: https://doi.org/10.1190/1.1443534.

BARBOSA, V. C. F.; SILVA, J. B. C.; MEDEIROS, W. E., 1997a," Gravity inversion of basement relief using approximate equality constraints on depths", *GEOPHYSICS*, 62, 1745–1757, doi: 10.1190/1.1444275.

BARBOSA, V. C. F.; SILVA, J. B. C.; MEDEIROS, W. E., 1999b, "Stable inversion of gravity anomalies of sedimentary basins with nonsmooth basement reliefs and arbitrary density contrast variations", *GEOPHYSICS*, 64, 754–764, doi: 10.1190/1.1444585.

BARBOSA, V. C. F.; SILVA, J. B. C.; MEDEIROS, W. E., 2002, "Practical applications of uniqueness theorems in gravimetry, part II: pragmatic

incorporation of concrete geologic information", *GEOPHYSICS*, 67, 795–80, doi: 10.1190/1.1484523.

BARBOSA, V. C. F.; SILVA, J. B. C., 2006, "Interactive 2D magnetic inversion: A tool for aiding forward modeling and testing geologic hypotheses", *GEOPHYSICS*, 71, no. 5, L43–L50, doi:10.1190/1.2258093.

BARNES, G.; BARRAUD, J., 2012, "Imaging geologic surfaces by inverting gravity gradient data with depth horizons", *GEOPHYSICS*, 77, no. 1, G1–G11, doi: 10.1190/geo2011-0149.1.

BHATTACHARYYA, B. K., 1964, "Magnetic anomalies due to prism-shaped bodies with arbitrary polarization", *GEOPHYSICS*, 29, 517-531, doi https://doi.org/10.1190/1.1439386.

BHATTACHARYYA, B. K., AND LEU, L. K., 1977, "Spectral analysis of gravity and magnetic anomalies due to rectangular prismatic bodies", GEOPHYSICS, 41, 41–50, doi: https://doi.org/10.1190/1.1440712.

BOTT, M. H. P., 1960, "The use of rapid digital computing methods for direct gravity interpretation of sedimentary basins", *Geophysical Journal of the Royal Astronomical Society*, 3, 63–67, doi: 10.1111/j.1365-246X.1960.tb00065.x.

CARATORI, T. F.; FAGGIONI, O.; BEVERINI, N.; CARMISCIANO, C., 2003, "Gaussian envelope for 3D geomagnetic data inversion", *GEOPHYSICS*, 68, 996-1007, doi: 10.1190/1.1581071.

CARATORI, T. F.; COCCHI, L.; CARMISCIANO, C., 2008, "Potential-field inversion for a layer with uneven thickness: The Tyrrhenian Sea density model", *Physics of the Earth and Planetary Interiors*, 166, 105-111.

CARVALHO J.; MATIAS, H.; RABEH, T.; MENEZES, P. T. L., BARBOSA, V. C. F.; DIAS, R.; CARRILHO, F., 2012," Connecting onshore structures in the Algarve with the southern Portuguese continental margin: The Carcavai fault zone", *Tectonophysics*, 570–571, 151–162, doi: 10.1016/j.tecto.2012.08.011.

CHRISTENSEN, A. N.; DRANSFIELD, M. H., 2002, “Airborne vector magnetometry over banded iron-formations”, *72nd Annual International Meeting, Society of Exploration Geophysicists*: Expanded Abstracts.

COSTA, J. B. S.; HASUI, Y.; BEMERGUY, R. L.; SOARES-JUNIOR, A. V.; VILEGAS, J. M. M., 2002, “Tectonics and paleogeography of the Marajo Basin, northern Brazil”, *Annals of the Brazilian Academy of Sciences*, 74, no. 3, 519-531.

DAMPNEY, C. N. G., 1969, “The equivalent source technique”, GEOPHYSICS, 34, no. 1, P39-53, doi: https://doi.org/10.1190/1.1439996.

DANNEMILLER, N.; LI, Y., 2006, “A new method for estimation of magnetization direction”, *GEOPHYSICS*, 71, no. 6, L69–L73, doi: 10.1190/1.2356116.

DRANSFIELD, M.; CHRISTENSEN, A.; LIU, G., 2003, “Airborne vector magnetics mapping of remanently magnetized banded iron formations at Rocklea, Western Australia”, *Exploration Geophysics*, 34, 93–96, doi: 10.1071/EG03093.

FARQUHARSON, C. G., 2008, “Constructing piecewise-constant models in multidimensional minimum-structure inversions”, *GEOPHYSICS*, 73, no. 1, K1– K9, doi: 10.1190/1.2816650.

FEDI, M.; FLORIO, G.; RAPOLLA, A., 1994, “A method to estimate the total magnetization direction from a distortion analysis of magnetic anomalies”, *Geophysical Prospecting*, 42, 261–274, doi:10.1111/j.1365-2478.1994.tb00209.x.

GALLARDO-DELGADO, L. A.; PÉREZ-FLORES, M. A.; GÓMEZ-TREVIÑO, E., 2003, “A versatile algorithm for joint 3D inversion of gravity and magnetic data”, *GEOPHYSICS*, 68, 949–959.

GEROVSKA, D.; ARAÚZO-BRAVO, M. J.; STAVREV, P., 2009, “Estimating the magnetization direction of sources from southeast Bulgaria through correlation between reduced-to-the-pole and total magnitude anomalies”, *Geophysical Prospecting*, 57, 491–505, doi:10.1111/j.1365-2478.2008.00761.x.

GUSPI, F., 1993, “Noniterative nonlinear gravity inversion”, *GEOPHYSICS*, 58, 935–940.

HANEY, M. M.; JOHNSTON, C.; LI, Y.; NABIGHIAN, M. N., 2003, “Envelopes of 3D and 3D magnetic data and their relationship to the analytic signal: Preliminary results”, *73rd Annual International Meeting, SEG, Expanded Abstracts*, 592–595.

HANSEN, P. C., 1992, “Analysis of discrete ill-posed problems by means of the L-curve”, SIAM Review”, 34, 561-580.

HIDALGO-GATO, M. C.; BARBOSA, V. C. F., 2015, “Edge detection of potential-field sources using scale-space monogenic signal: Fundamental principles”, *GEOPHYSICS*, 80, no. 5, J27-J36, doi: 10.1190/GEO2015-0025.1.

HIDALGO-GATO, M. C.; BARBOSA, V. C. F., 2019, “Fast 3D magnetic inversion of a surface relief in the space domain”, *GEOPHYSICS*, 84, no. 5, 1–11, doi: 10.1190/GEO2018-0712.1.

IALONGO, S.; FEDI, M.; FLORIO, G., 2014, “Invariant models in the inversion of gravity and magnetic fields and their derivatives”, *Journal of Applied Geophysics*, 110, 51–62, doi: http://dx.doi.org/10.1016/j.jappgeo.2014.07.023.

LI, Y.; OLDENBURG, D. W.; 1996, “3-D inversion of magnetic data”, *GEOPHYSICS*, 61, 394–408, doi:10.1190/1.1443968.

LI, Y.; SHEARER, S. E.; HANEY; M. M., DANNEMILLER, N., 2010, “Comprehensive approaches to 3D inversion of magnetic data affected by remanent magnetization”, *GEOPHYSICS*, 75, no. 1, L1–L11, doi: 10.1190/1.3294766.

LOURENCO J.; MENEZES, P. T. L.; BARBOSA V. C. F., 2014, “Connecting onshore-offshore Campos Basin structures: Interpretation of high-resolution airborne magnetic data”, *Interpretation*, 2, p. SJ181–SJ191, doi: 10.1190/INT-2014-0007.1.

LOURENCO, J. S.; MORRISON, H. F., 1973, “Vector magnetic anomalies derived from measurements of a single component of the field”, *GEOPHYSICS*, 38, 359–368.

MARQUARDT, D. W., 1963, “An algorithm for least-squares estimation of nonlinear parameters”, *Journal of the Society for Industrial and Applied Mathematics*, 11, 431–441.

MARTINS, C. M.; LIMA, W. A.; BARBOSA, V. C. F.; SILVA, J. B. C., 2011, “Total variation regularization for depth-to-basement estimate, Part 1: Mathematical details and applications”, *GEOPHYSICS*, 76, no. 1, I1–I12, doi: 10.1190/1.3524286.

MEDEIROS, W. E.; SILVA, J. B. C., 1995, “Simultaneous estimation of total magnetization direction and 3-D spatial orientation”, *GEOPHYSICS*, 60, 1365–1377, doi:10.1190/1.1443872.

MICKUS, K. L.; PEEPLES, W. J., 1992, “Inversion of gravity and magnetic data for the lower su rface of a 2.5-dimensional sedimentary basin”, *Geophysical Prospecting*, 40, 171–193, doi: 10.1111/j.1365-2478.1992.tb00370.x.

NABIGHIAN, M. N., 1972, “The analytic signal of two-dimensional magnetic bodies with polygonal cross-section: Its properties and use for automated anomaly interpretation”, *GEOPHYSICS*, 37, 507–517, doi: 10.1190/1.1440276.

NABIGHIAN, M. N., 1984, “Toward a three-dimensional automatic interpretation of potential field data via generalized Hilbert transforms: Fundamental relations”, *GEOPHYSICS*, 49, 780–786, doi: 10.1190/1.1441706.

NUNES, T. M.; BARBOSA, V. C. F.; SILVA, J. B. C., 2008, “Magnetic Basement Depth Inversion in the Space Domain”, *Pure and Applied Geophysics*, 165, 1891–1911, doi: 10.1007/s00024-008-0405-x.

OKUBO, Y.; GRAFT, R. J.; HANSEN, R. O.; OGAWA, K.; TSU, H., 1985, “Curie depths of the Island of Kyushu and surrounding areas, Japan”, *GEOPHYSICS*, 53, 481-494, doi: https://doi.org/10.1190/1.1441926.

OLDENBURG, D.W., 1974, “The inversion and interpretation of gravity anomalies”, *GEOPHYSICS*, 39, 526–536, doi: 10.1190/1.1440444.

OLIVEIRA JR., V. C.; BARBOSA, V. C. F.; SILVA, J. B. C., 2011, “Source geometry estimation using the mass excess criterion to constrain 3-D radial inversion of

gravity data", *Geophysical Journal International*, 187, 754–772, doi: 10.1111/j.1365-246X.2011.05172.x.

OLIVEIRA JR., V. C.; BARBOSA, V. C. F., 2013, "3-D radial gravity gradient inversion", *Geophysical Journal International*, 195, 883–902, doi: 10.1093/gji/ggt307.

OLIVEIRA JR., V. C.; SALES, D. P.; BARBOSA, V. C. F.; UIEDA, L., 2015, "Estimation of the total magnetization direction of approximately spherical bodies", *Nonlinear Processes in Geophysics*, 22, 215–232, doi:10.5194/npg-22-215-2015.

PARKER, R. L., 1973, "The rapid calculation of potential anomalies", *Geophysical Journal of the Royal Astronomical Society*, 31, 447–455.

PARKER, R. L.; SHURE, L.; HILDEBRAND, J. A., 1987, "The application of inverse theory to seamount magnetism". *Reviews of Geophysics*, 25, 17-40.

PEDERSEN, L. B., 1978, "Wavenumber domain expressions for potential fields from arbitrary 2-, 2-1/2-, and 3-dimensional bodies", *GEOPHYSICS*, 43, 626–630, doi: 10.1190/1.1440841.

PHILLIPS, J. D., 2005, "Can we estimate total magnetization directions from aeromagnetic data using Helbig's integrals?", *Earth Planets Space*, 57, 681–689.

PILKINGTON, M., 2016, "Resolution measures for 3D magnetic inversions", *GEOPHYSICS*, 81, no. 2, J1-J9, doi: 10.1190/GEO2015-0081.1.

PORTNIAGUINE, O.; ZHDANOV, M. S., 2002, "3-D magnetic inversion with data compression and image focusing", *GEOPHYSICS*, 67, 1532–1541, doi: 10.1190/1.1512749.

SHEARER, S.; LI, Y., 2004, "3D inversion of magnetic total gradient data in the presence of remanent magnetization", *74th Annual International Meeting, SEG, Expanded Abstracts*, 774–777.

SILVA, J. B. C.; MEDEIROS, W. E.; BARBOSA, V. C. F., 2001, "Pitfalls in nonlinear inverse problem", *Pure and Applied Geophysics*, 158, 945–964, doi: 10.1007/PL00001215.

SILVA DIAS, F. J. S.; BARBOSA, V. C. F.; SILVA, J. B. C., 2007, "2D gravity inversion of a complex interface in the presence of interfering sources", *GEOPHYSICS*, 72, no. 2, I13–I22, doi: 10.1190/1.2424545.

SILVA, J. B. C.; SANTOS, D. F.; GOMES, K. P., 2014, "Fast basement relief inversion", *GEOPHYSICS*, 79, no. 5, G79–G91, doi: 10.1190/GEO2014-0024.1.

SILVA DIAS, F. J. S.; BARBOSA, V. C. F.; SILVA, J. B. C., 2009, "3D gravity inversion through an adaptive-learning procedure", *GEOPHYSICS*, 74, no. 3, I9–I21, doi:10.1190/1.3092775.

SILVA DIAS, F. J. S.; BARBOSA, V. C. F.; SILVA, J. B. C., 2011, "Adaptive learning 3D gravity inversion for salt-body imaging", *GEOPHYSICS*, 76, no. 3, I49–I57, doi: 10.1190/1.3555078.

SPECTOR, A.; GRANT, F. S., 1970, "Statistical models for interpreting aeromagnetic data", *GEOPHYSICS*, 35, 293–302, doi:10.1190/1.1440092.

SKEELS, D. C., 1947, "Ambiguity in gravity interpretation", *GEOPHYSICS*, 12, 43–56, doi: 10.1190/1.1437295.

RICHARDS, M. L.; VACQUIER, V.; VAN VOORHIS, G. D., 1967, "Calculation of the magnetization of uplifts from combining topography and magnetic surveys", *GEOPHYSICS*, 32, 678-707, doi: https://doi.org/10.1190/1.1439883.

TIKHONOV, A. N.; ARSENIN, V. Y., 1977, "Solutions of ill-posed problems", *W. H. Winston & Sons*.

UIEDA, L.; BARBOSA, V. C. F., 2012, "Robust 3D gravity gradient inversion by planting anomalous densities", *GEOPHYSICS*, 77, no. 4, G55–G66, doi: 10.1190/geo2011-0388.1.

UIEDA, L.; OLIVEIRA JR, V. C.; BARBOSA, V. C. F., 2013, "Modeling the Earth with Fatiando a Terra: techniques", *12th Python in Science Conference, SCIPY 2013*, Proceedings, 90–96.

UIEDA, L.; BARBOSA, V. C. F.; BRAITENBERG, C., 2016, "Tesseroids: forward-modeling gravitational fields in spherical coordinates", *GEOPHYSICS*, 81, no. 5, F41–F48, doi: 10.1190/GEO2015-0204.1.

UIEDA, L.; BARBOSA, V. C. F., 2017, “Fast nonlinear gravity inversion in spherical coordinates with application to the South American Moho”, *Geophysical Journal International*, 208, 162–176, doi: 10.1093/gji/ggw390.

ZALAN, P. V., 2017, “The Differential Petroleum Potential of the Spectrum of Types of Passive Margins”, SBGf, 15th International Congress of the Brazilian Geophysical Society.

ZEYEN, H.; POUS, J., 1991, “A new 3-D inversion algorithm for magnetic total field anomalies”, *Geophysical Journal International*, 104, 583–591, doi: 10.1111/j.1365-246X.1991.tb05703.